



Full Length Article

Pulsed reverse electrochemical synthesis of Ag-TiO₂ composites from deep eutectic solvents: Photocatalytic and antibacterial behaviour

Ionela-Cristina Petcu^a, Raluca Negrea^{b,c}, Ana T.S.C. Brandão^d, Cosmin Romanitan^e, Oana Brincoveanu^e, Nikolay Djourellov^f, Iuliana Mihalache^e, L. Monica Veca^e, Gabriela Isopencu^a, Carlos M. Pereira^d, Liana Anicai^g, Cristina Busuioc^{a,*}, Sabrina State (Rosoiu)^{e,h,*}

^a Faculty of Chemical Engineering and Biotechnologies, National University for Science and Technology POLITEHNICA Bucharest, 1-7 Gheorghe Polizu Street, 011061 Bucharest, Romania

^b Brunel University London, Kingston Lane, Uxbridge, UB8 3PH, United Kingdom

^c National Institute of Materials Physics, Atomistilor 405A, 077125 Magurele, Romania

^d CIQUP/IMS - Chemistry Research Center, Faculty of Sciences, University of Porto, Rua do Campo Alegre 1021, 4169-007 Porto, Portugal

^e National Institute for Research and Development in Microtechnologies - IMT Bucharest, 126a Erou Iancu Nicolae, 077190 Bucharest, Romania

^f Extreme Light Infrastructure - Nuclear Physics Horia Hulubei National Institute for Physics and Nuclear Engineering, 30, Reactorului Street, 077125 Magurele, Ilfov county, Romania

^g Center for Surface Science and Nanotechnology- National University for Science and Technology POLITEHNICA Bucharest, 1-7 Gheorghe Polizu Street, 011061 Bucharest, Romania

^h Faculty of Medical Engineering, National University for Science and Technology POLITEHNICA Bucharest, 1-7 Gheorghe Polizu Street, 011061 Bucharest, Romania

ARTICLE INFO

Keywords:

Pulsed reverse current electrodeposition
Deep eutectic solvent
Ag-tio2 composite
Photocatalytic activity
Antibacterial effect

ABSTRACT

This study presents an environmentally friendly approach for synthesis Ag-TiO₂ composite using pulsed reverse current (PRC) electrodeposition from green electrolytes, specifically deep eutectic solvents (DESS). The combination of PRC and DESS offers better control over nanoparticle synthesis while eliminating the need for toxic or expensive precursors, representing a significant advancement in sustainable nanomaterial synthesis. Different electrochemical parameters were adjusted, and their influence on the structure and morphology of the composite was investigated using X-ray diffraction (XRD), X-ray photoelectron spectroscopy (XPS), scanning electron microscopy (SEM) and transmission electron microscopy (TEM). TEM analysis revealed that silver nanoparticles (Ag NPs) are attached to TiO₂ nanopowder, with the coexistence of TiO₂ and Ag further confirmed by XRD and XPS. The recorded UV-Vis diffuse reflectance spectra (DRS) displayed a broad peak in the range of 400 – 650 nm, associated with the localized surface plasmon resonance (LSPR) of Ag NPs on the semiconductor's surface. The photocatalytic activity of TiO₂ nanopowder and Ag-TiO₂ composite was evaluated based on the degradation of methyl orange (MO) dye under UV and visible light illumination. Our findings clearly demonstrated that the incorporation of Ag improved the photocatalytic efficiency. The mechanism of MO dye degradation was explored by using various scavengers, revealing that superoxide radicals ($\bullet\text{O}_2^-$) play a dominant role. Furthermore, the incorporation of Ag NPs significantly enhanced the antimicrobial activity of the oxide against both Gram-positive (*B. subtilis*) and Gram-negative (*E.coli*) strains.

1. Introduction

Among the various semiconductor oxides with remarkable photocatalytic activity, titanium dioxide (TiO₂) has been extensively studied for the photodegradation of organic and inorganic pollutants due to its low cost and non-toxicity [1]. Among the many organic water

pollutants, methyl orange (MO) is a carcinogenic azo dye widely used in industries such as textiles, foodstuffs, paper and leather [2]. It is water-soluble and possesses high chemical stability and low biodegradability, making it difficult to remove using conventional water purification methods. The toxic effects of MO on human health are well-documented, as its presence in drinking water can cause

* Corresponding authors.

E-mail addresses: crisrina.busuioc@upb.ro (C. Busuioc), sabrina.rosoiu@upb.ro (S.S. (Rosoiu)).

<https://doi.org/10.1016/j.apsadv.2025.100749>

Available online 21 April 2025

2666-5239/© 2025 The Authors. Published by Elsevier B.V. This is an open access article under the CC BY-NC-ND license (<http://creativecommons.org/licenses/by-nc-nd/4.0/>).

headache, anemia, abdominal pain, nausea, dizziness, and confusion. Prolonged exposure at high levels can even be fatal [2–4]. Therefore, its removal from water is a major concern. However, the practical application of TiO₂ for the photodegradation of organic dyes is limited to the ultraviolet (UV) region due to its wide band gap (~3.2 eV), which allows it to utilize only about 5 % of solar energy, compared to visible light, which constitutes approximately 50 % [5,6].

Different approaches have been investigated to improve the TiO₂ photocatalytic activity under visible light [6–8]. Among them, Ag incorporation represents an effective strategy, as it extends the light absorption of TiO₂ in the visible region due to the LSPR effect [10–14]. Additionally, it improves the photocatalytic efficiency of the oxide by forming a high Schottky barrier at the metal-TiO₂ interface, which act as an electron trap, preventing electron-hole recombination after photon absorption [9,10]. Furthermore, Ag exhibits a broad-spectrum antibacterial activity, improving the bactericidal performance of TiO₂ [5, 11–14]. The antibacterial properties of Ag-TiO₂ composites have been attributed to the synergistic effect of silver ions, released from the dissolution of Ag NPs, and the production of reactive species by the photocatalyst. These reactive species disrupt the integrity of the bacterial cell membranes, causing leakage of intracellular components and ultimately leading to cell death [15,16]. Ag-TiO₂ composites have demonstrated effectiveness against a wide range of Gram-positive (*Bacillus subtilis*, *Staphylococcus aureus*, MRSA) and Gram-negative (*Escherichia coli*, *Klebsiella pneumoniae*, *Pseudomonas aeruginosa*) bacterial strains, as well as fungi (*Candida albicans*) [14]. The potential applications of Ag-TiO₂ composites include environmental remediation owing to their photocatalytic activity against organic pollutants and pharmaceutical compounds, as well as biological applications due to their antibacterial, antiviral and antifungal properties [13,17–23].

Various methods have been reported for synthesizing Ag-TiO₂ composites, including hydro/solvothermal [20,24], sol-gel [25–28], chemical reduction [29] and co-precipitation [30] among others [18,23]. Mao et al. reported the hydrothermal synthesis of Ag-TiO₂ composites with different Ag loading (5 %, 10 %, 20 % and 40 %) and investigated their efficiency in the photodegradation of MO [24]. Among the different samples, 20 % Ag-TiO₂ composite exhibited the highest photodegradation efficiency. In another study, Harikishore and co-authors reported the synthesis of Ag-TiO₂ composite by sol-gel route [27]. The authors used titanium tetra n-butoxide as a precursor, which was mixed with acetic acid and silver nitrate solution in water (5 mol %) for 8 h to obtain a transparent sol that was further dried and annealed for 5 h. The incorporation of Ag into TiO₂ reduced the band gap of the semiconductor, enhanced its photocatalytic activity for the degradation of methylene blue (MB) dye under UV light, and significantly improved its antibacterial properties against the Gram-negative strain, *E. coli* (*E. coli*).

Despite these advancements, many conventional synthesis methods remain costly, require long processing times, and rely on toxic precursors [9,18,26]. Electrochemical routes offer several advantages, including cost-effectiveness, scalability and high purity materials, making them highly suitable for various industrial applications [31–34]. Among electrochemical techniques, pulsed reversed current electrodeposition (PRC) stands out for its versatility [35–37]. PRC enables precise tuning of deposition parameters such as pulse duration, frequency, duty cycle, current density and deposition time, allowing better control over NPs size, shape and distribution [38,39]. In contrast, sol-gel and hydrothermal methods primarily depend on temperature and precursor ratios, which can lead to inconsistent morphology [40]. In recent years, deep eutectic solvents (DESs) have gained significant attention as an eco-friendly alternative electrolyte in nanomaterials synthesis, further supporting global sustainability goals [41]. DESs consist of a mixture of a hydrogen bond donor (HBD) with a hydrogen bond acceptor (HBA), in a specific ratio, resulting in a solution with a melting point lower than that of its individual components [42]. Their advantages include lower cost, biodegradability, non-toxicity, high viscosity, low vapor-pressure, and tunability. DESs have revolutionized nanomaterial synthesis, as

their properties facilitate control over morphology, dimension, and surface characteristics [43]. Moreover, the combination of DESs, as green electrolytes, with PRC provides a cost-effective and environmentally friendly approach to nanomaterial synthesis, eliminating the need for expensive or hazardous precursors. Previously, we successfully reported the decoration of multi-walled carbon nanotubes (MWCNTs) with Ag-NPs via PRC from a DESs based on a mixture of choline chloride and glycerol (1:2 molar ratio) for energy storage applications [44]. During the electrochemical synthesis, the pulse duration of the anodic and cathodic phases was varied, while the off-time between pulses remained fixed. The size of the Ag-NPs depended on the selected electrochemical parameters. The decoration of the MWCNTs with Ag significantly improved the capacitance retention of the modified MWCNTs electrodes.

The novelty of this work lies in the synthesis of an Ag-TiO₂ composite using an approach that combines deep eutectic solvents (DESs), based on a choline chloride-ethylene glycol mixture, with the pulsed reversed current (PRC) electrodeposition method. This synthesis route allows for the tuning of deposition parameters, resulting in the formation of well-defined Ag NPs on TiO₂, while offering a cost-effective and environmentally friendly alternative to conventional synthesis methods. The influence of the PRC parameters on the crystallite size, Ag loading, morphology, and photocatalytic activity for MO degradation under UV and visible light irradiation was analysed. To understand the mechanism of MO dye degradation, various scavengers were used, and its mineralization was studied. Furthermore, the antimicrobial activity of the optimized Ag-TiO₂ photocatalyst was investigated against Gram-positive (*B. subtilis var spizizenii*) and Gram-negative (*E.coli*) strains. Clearly, Ag incorporation improved both the photocatalytic and bactericidal activity of the semiconductor.

2. Materials and methods

2.1. Chemicals and preparation of DESs

All chemicals, namely choline chloride (ChCl ≥ 98 %, Thermo Scientific), ethylene glycol (EG, ≥ 99 %, Thermo Scientific), poly (N-vinyl pyrrolidone) (PVP 10, Sigma Aldrich), tetrabutylammonium bromide (TBAB, ≥ 98 %, Sigma Aldrich), ethanol (EtOH), and methyl orange (MO, Polymed Trade, Bucharest, Romania), were used as received. The DES, named ILEG, was prepared by mixing and heating ChCl with EG in a 1:2 molar ratio at 70 °C until a homogeneous and transparent liquid was formed.

2.2. Electrochemical synthesis of tio₂ and ag-tio₂

The electrochemical synthesis of TiO₂ nanopowder was performed using a procedure previously described by our group [45]. Briefly, a two-electrode configuration was used, with a pure titanium disk (surface = 36.3 cm²) as the sacrificial anode and a nickel foil (surface = 15.2 cm²) as the cathode. A 1:2 vol mixture of ILEG-EtOH, containing 5 mM TBAB to improve conductivity, was used as the electrolyte. TiO₂ nanopowder was synthesized under DC conditions at a fixed current density of 40 mA/cm² for 3 h. Following the electrochemical synthesis, 10 mL of deionized water was added to the electrolyte for hydrolysis, resulting in a white gel, which was subsequently cleaned by centrifugation with water and ethanol (4000 rpm, 15 min, repeated 4 times). Finally, the nanopowder was dried at 110 °C for 1 h and calcinated at 600 °C for 2 h.

In another series of experiments, Ag-TiO₂ composites were prepared by PRC using the 'sacrificial anode' method. First, 5 g/L of PVP was dissolved in the ILEG electrolyte. Subsequently, 12 g/L of electrochemically prepared TiO₂ nanopowder was added and dispersed by stirring. The setup consisted of two silver wires (≥ 99.99 %, 5 cm² area, Sigma Aldrich) connected to a pulsed reverse power supply (pe86CB 3HE, plating electronic GmbH). Prior to each experiment, the Ag wires

Table 1
Pulsed plating parameters involved in the synthesis of Ag-TiO₂ composite.

| Sample | Anodic pulse (reverse) I_p^+ T_{on}^r | T_{off} | Cathodic pulse (forward) I_p^- T_{on}^f | Frequency f | Duty cycle θ | Overall time |
|--|---|-----------|---|---------------|---------------------|--------------|
| Ag-TiO ₂ -1.1 | +100 mA | 100 ms | -100 mA | 3.33 Hz | 0.67 | 1h |
| Ag-TiO ₂ -1.2 (further named Ag-TiO ₂ -1h) | 100 ms | 200 ms | 100 ms | 2.5 Hz | 0.5 | |
| Ag-TiO ₂ -1.3 | | 300 ms | | 2 Hz | 0.4 | |
| Ag-TiO ₂ -3h | +100 mA | 200 ms | -100 mA | 2.5 Hz | 0.5 | 3h |
| Ag-TiO ₂ -6h | 100 ms | 100 ms | 100 ms | | | 6h |

* I_p^+ - anodic peak current, I_p^- - cathodic peak current, T_{on}^r - anodic peak duration, T_{on}^f - cathodic peak duration and T_{off} - duration of the period during which no current is applied.

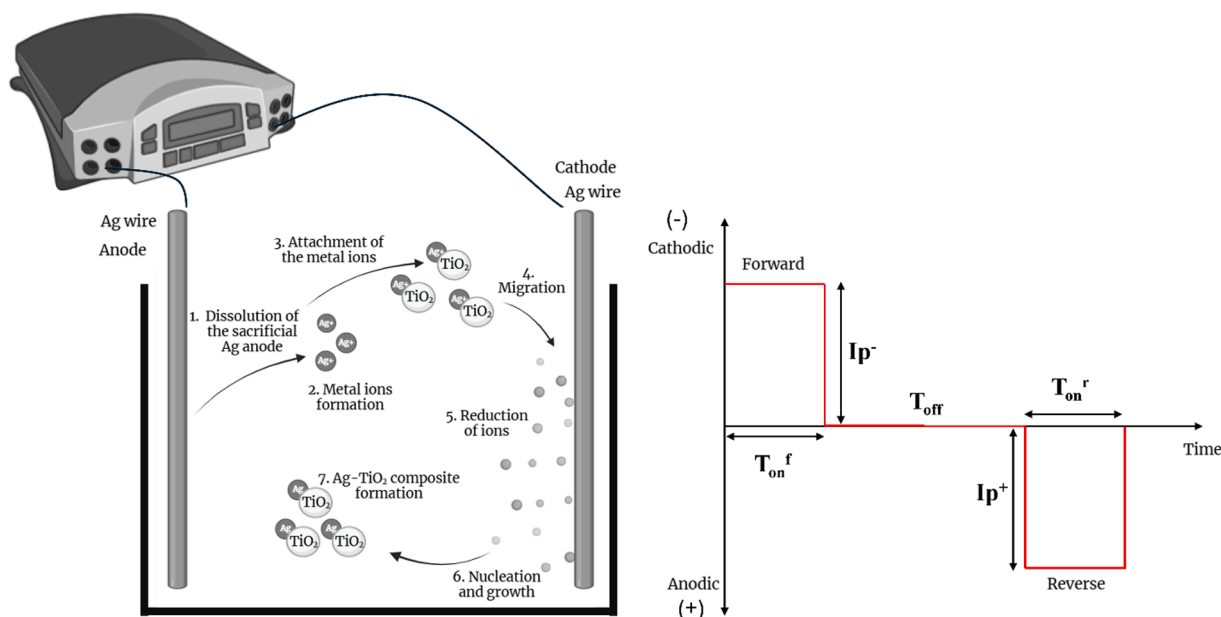


Fig. 1. Schematic of the electrochemical synthesis of the Ag-TiO₂ composite.

were mechanically polished. The PRC parameters studied are presented in Table 1, and a schematic representation of the setup and pulse plating wave is shown in Fig. 1. The duty cycle, θ , and frequency, f , were calculated according to the following equation [46]:

$$\theta = \frac{T_{on}^f + T_{on}^r}{T_{on}^f + T_{off} + T_{on}^r} \quad (1)$$

$$f = \frac{1}{T_{on}^f + T_{off} + T_{on}^r} \quad (2)$$

where T_{on}^f and T_{on}^r are the forward (cathodic) and reverse (anodic) times, respectively, while T_{off} is the time during which zero current is applied between the forward and reverse pulses.

The electrochemical synthesis was performed at room temperature under stirring. After the electrodeposition process, the suspension was cleaned by centrifugation with water and ethanol (4000 rpm, 15 min, repeated 4 times).

The selection of the PRC parameters was based on our expertise regarding pulse plating synthesis using DESs electrolytes [44,47–49]. Due to the relatively high viscosity of DESs compared to aqueous electrolytes, longer anodic and cathodic times, as well as extended T_{off} times, are required to facilitate metal ion diffusion. However, a key shortcoming of this synthesis method is the efficient removal of residual DESs from the nanocomposite. The high viscosity of the DESs makes their removal difficult, requiring thorough cleaning steps, including centrifugation with appropriate solvents (water and ethanol), to ensure the

purity of the final material.

2.3. Characterization

The morphology and composition of the electrochemically synthesized TiO₂ nanopowder and Ag-TiO₂ composite were assessed by field emission gun scanning electron microscopy (FEGSEM) using a Nova NanoSEM 630 (FEI) equipment operated at 10 kV, equipped with energy dispersive X-ray spectrometer (EDX) from Smart Insight AMETEK. The structure of the powders was investigated using an X-ray diffractometer from Rigaku SmartLab with a CuK α 1 source ($\lambda = 0.15406$ nm), operating at room temperature in the 2θ range of 10–70°. Peak indexing was performed with the help of the International Centre Diffraction Data (ICDD) database. The surface area and the porosity of the samples were determined using a Brunauer-Emmett-Teller nitrogen adsorption analyzer (BET, TriStar Plus, Micromeritics, Norcross, GA, USA). Diffuse reflectance spectra (DRS) were recorded between 250 and 650 nm using a JASCO V-770 spectrophotometer equipped with an integrating sphere. X-ray photoelectron spectroscopy (XPS) spectra were recorded on a Sigma Surface Science photoelectron spectrometer equipped with a 160-mm hemispherical energy analyzer with a 1D detector (ASPECT), using a poly-chromatic Al X-ray source at 13 kV and a power of 200 W. The analysis area was 1.3×1.3 mm². The analysis was performed by CasaXPS software [50]. All spectra were fitted using a Shirley-type background and a Lorentzian-Gaussian peak shape. For calibration of the binding energy spectra, the C 1 s component associated to C–C peak, adjusted to 248.8 eV, was used as a reference. All TEM analyses,

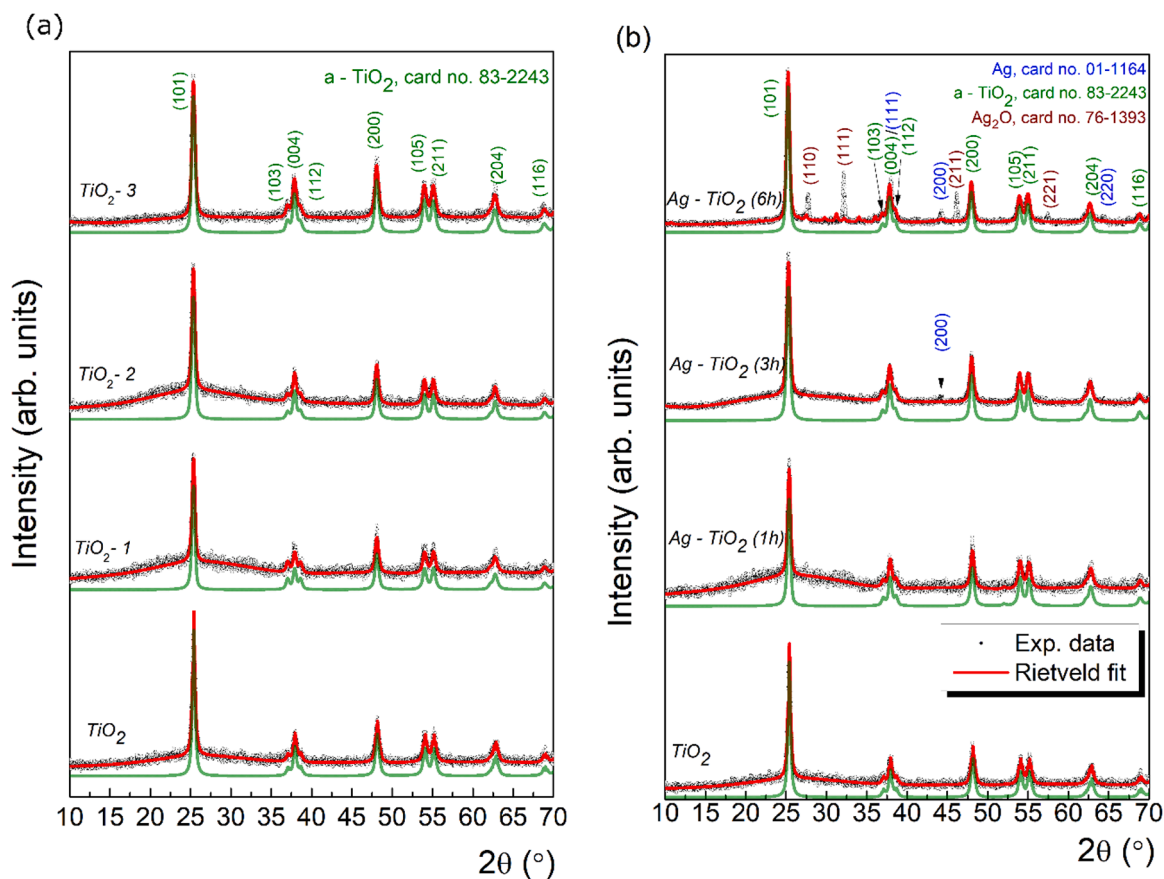


Fig. 2. Experimental XRD data (black points), database pattern for anatase-TiO₂ used for Rietveld refinement (green line), and final Rietveld fit (red line) for TiO₂ and Ag-TiO₂ composites: (a) TiO₂, Ag-TiO₂-1.1, Ag-TiO₂-1.2 and Ag-TiO₂-1.3; (b) TiO₂, Ag-TiO₂-1 h, Ag-TiO₂-3 h and Ag-TiO₂-6 h.

Table 2

Results of the Rietveld refinements obtained for TiO₂ and Ag-TiO₂ composites.

| Sample | Unit cell parameters (nm) – TiO ₂ | Mean crystallite size (nm) – TiO ₂ | Lattice strain (%) – TiO ₂ |
|---|--|---|---------------------------------------|
| TiO ₂ | $a = b = 0.37; c = 0.95$ | 27.3 | +0.43 |
| Ag-TiO ₂ – 1.1 | $a = b = 0.37; c = 0.95$ | 19.9 | +0.36 |
| Ag-TiO ₂ – 1.2 (or Ag-TiO ₂ -1h) | $a = b = 0.37; c = 0.95$ | 15.8 | +0.36 |
| Ag-TiO ₂ – 1.3 | $a = b = 0.37; c = 0.95$ | 17.4 | +0.41 |
| Ag-TiO ₂ -3h | $a = b = 0.37; c = 0.95$ | 14.3 | +0.13 |
| Ag-TiO ₂ -6h | $a = b = 0.37; c = 0.95$ | 17.3 | +0.06 |

including Conventional TEM (CTEM), Selected Area Electron Diffraction (SAED), High-Resolution TEM (HRTEM), Scanning TEM (STEM), and Energy Dispersive X-ray Spectroscopy (EDS), were performed using a SPECTRA 300 TEM from Thermo Fisher (Brunel University of London, UK). The instrument is equipped with a Super-X EDS detector for chemical analysis and operated at 200 kV to prevent sample damage. The samples for TEM analysis were prepared by dispersing the powders in ethanol, and two drops of the solution were deposited onto gold grids coated with carbon membrane. The STEM image simulation was performed using TEMPAS software from Total Resolution LLC, while Vesta software was used for atomic model visualization.

2.4. Photocatalytic experiments

The photoreactivity of the TiO₂ and Ag-TiO₂ composites was evaluated under UV irradiation ($\lambda = 365$ nm, 6 W, Wiesloch) and visible light illumination (LSH-7320, ORIEL solar simulator, 100 mW/cm²) for the

degradation of MO dye (10 mg/mL) at pH=3. For the experiments, 1 g/L of nanopowder was added to 25 mL of the dye solution, followed by exposure to UV radiation or visible light under continuous stirring. Prior to irradiation, the samples were magnetically stirred in the dark for 30 min to establish the adsorption equilibrium. The residual dye concentration was quantified every hour in 3 mL aliquots using the absorption maxima of the chromophore at 504 nm to evaluate the degradation efficiency. The absorption spectra were recorded in the wavelength range of 200 - 800 nm using an UV-VIS spectrophotometer (Agilent Cary 5000). Before spectroscopy analysis, the samples were centrifuged at 4000 rpm for 5 min to remove the powder.

For the investigation of the mechanism of MO dye removal, ethylenediaminetetraacetic acid disodium (Na₂EDTA), isopropanol (IPA) and benzoquinone (BQ) were used as capture agents for holes (h^+), hydroxyl radical ($\bullet OH$), and superoxide radical ($\bullet O_2^-$) respectively. Ag-TiO₂-3 h (1 g/L and 25 mL of 10 mg/mL MO dye solution) was stirred in the dark for 30 min to allow the system to reach the adsorption equilibrium. After, 0.5 mL of 0.1 mol/L of the above-mentioned capture agents were added [51] and the absorption was measured after 7 h of exposure to UV radiation.

2.5. Antimicrobial activity

The antimicrobial activity of the samples was investigated against Gram-positive and Gram-negative strains. The microorganisms analyzed were the Gram-negative bacteria *E. coli* (DH5K strain) and *B. subtilis* var. *spizizenii* as Gram-positive bacteria, sourced from the microorganism collection of the Bioreactor Laboratory, FICBi. The Nutrient agar (NA) was used as the culture medium. The plates were inoculated with 100 μ L of microorganism suspension (OD 0.1201 at 600 nm for *E. coli* and

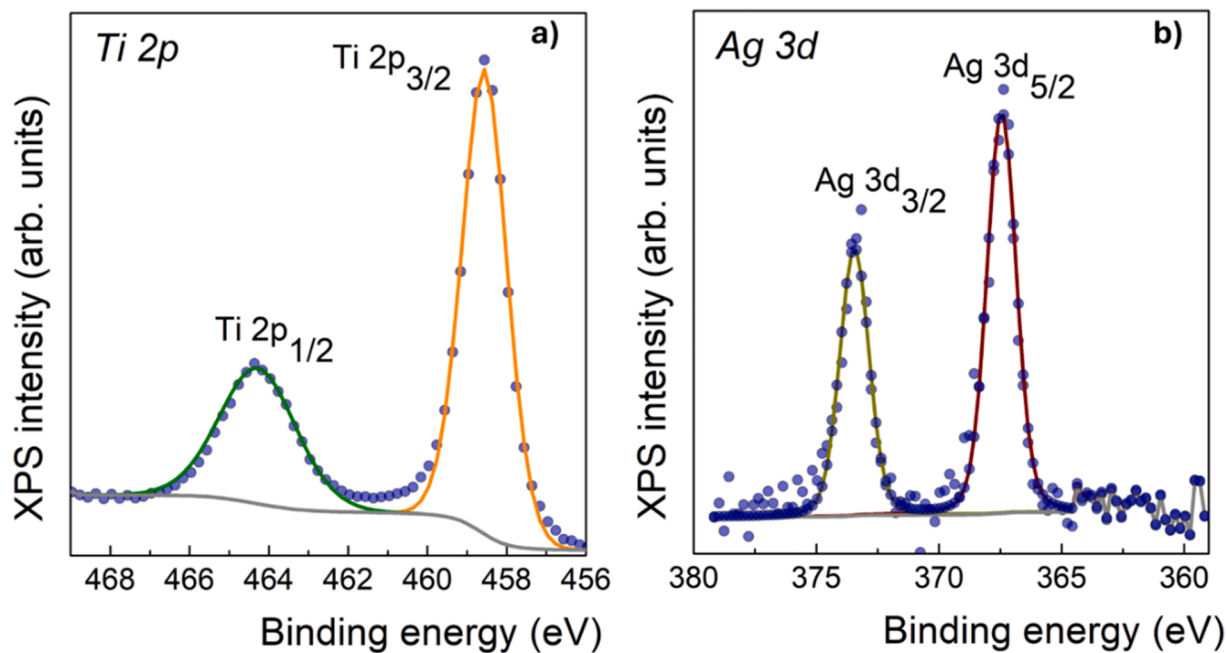


Fig. 3. XPS spectra for (a) Ti 2p and (b) Ag 3d corresponding to Ag-TiO₂-6 h sample.

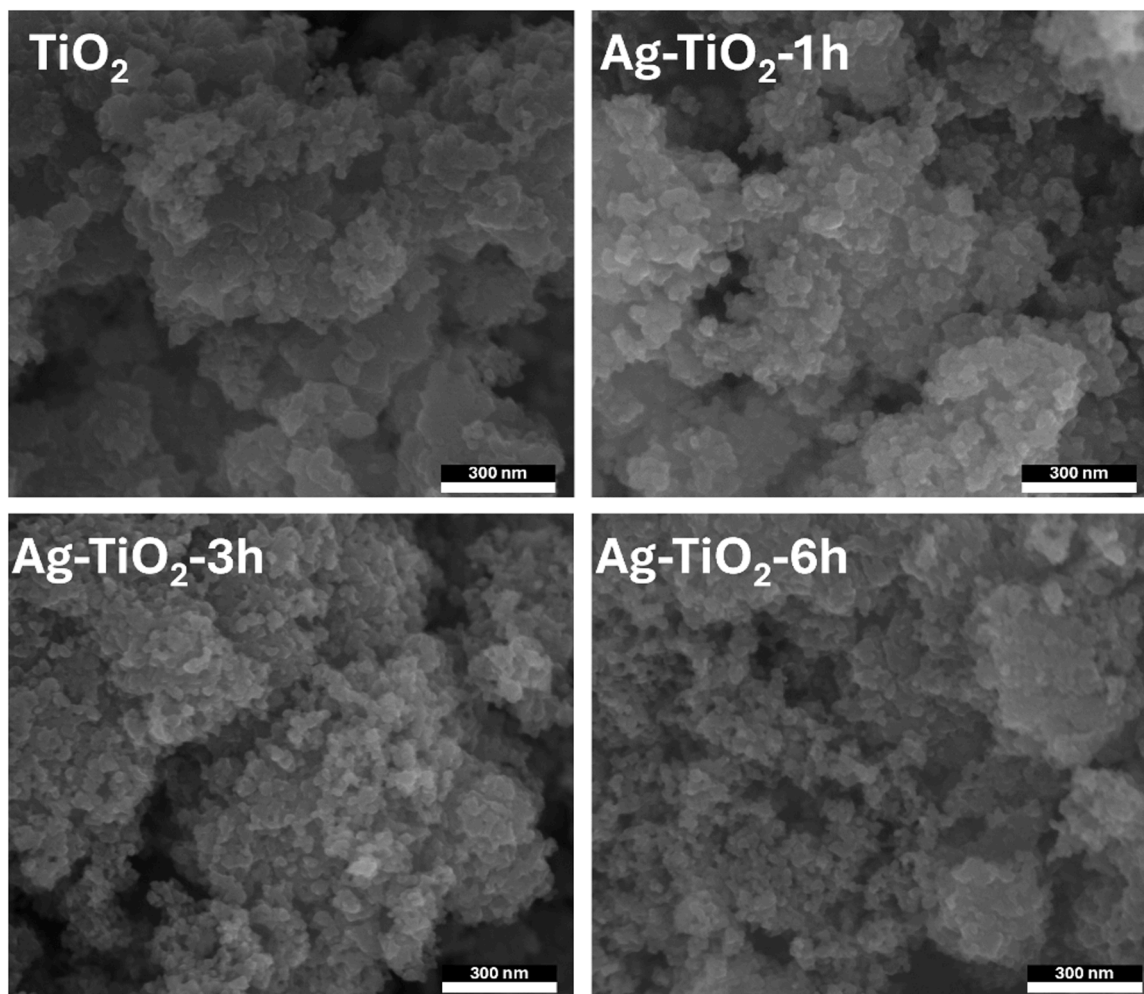


Fig. 4. SEM-micrographs of TiO₂ and Ag-TiO₂ composites: Ag-TiO₂-1 h, Ag-TiO₂-3 h and Ag-TiO₂-6 h.

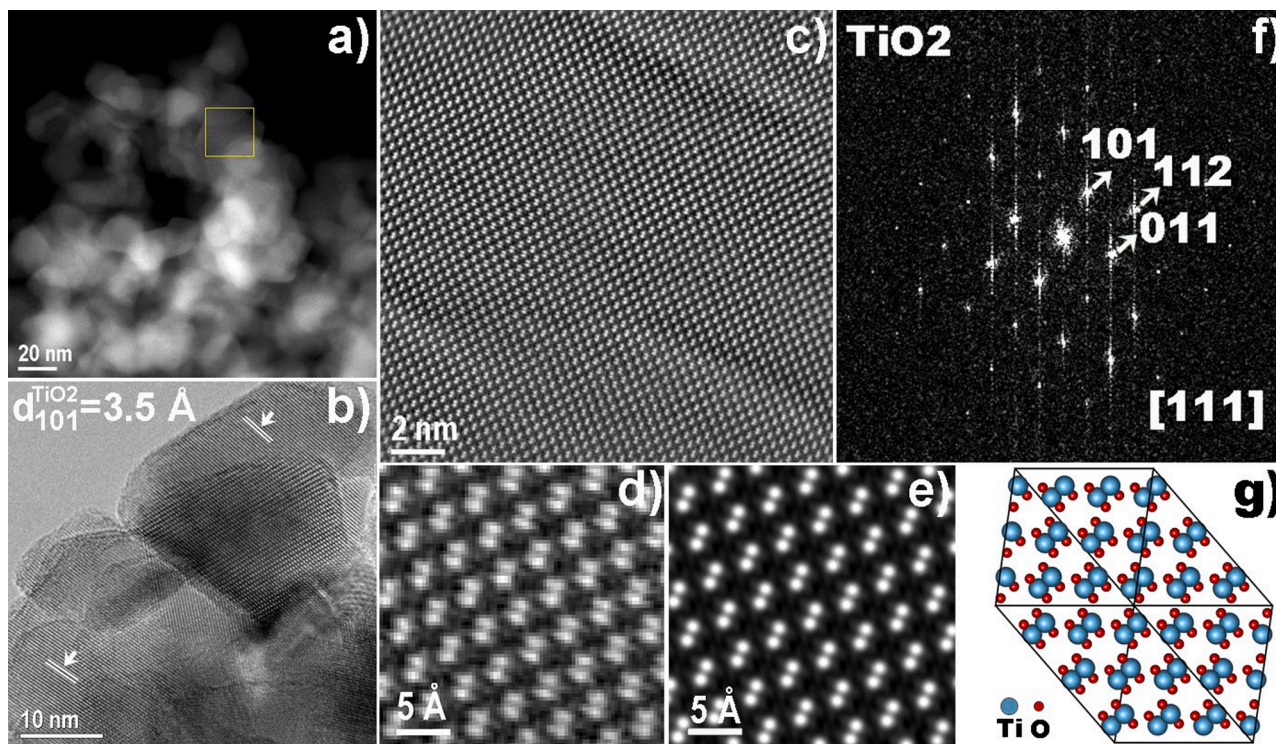


Fig. 5. (a) low-magnification STEM image and (b) HRTEM image of TiO₂ NPs; (c) and (d) STEM images at atomic level showing the atomic arrangement of TiO₂ anatase phase; (e) Simulated HAADF-STEM image; (f) FFT pattern corresponding to STEM image (c); and (g) atomic model of the anatase phase.

0.1158 for *B. subtilis*). After inoculation, the plates were left in the oven with controlled humidity for about 1 h to allow the bacterial suspension to uniformly impregnate the medium. Wells with a diameter of 6 mm were created on each plate. The powder to be analysed was sterilized under UV for 1 h (Model UVGL-58 Mineralight Lamp 254/365 nm), weighed, and aseptically distributed in the wells made on the plate. The result of the antimicrobial activity was expressed as the zone of inhibition (IZ, mm), represented by the clear zone surrounding the samples.

3. Results and discussion

3.1. Electrochemical synthesis and characterization

TiO₂ powder was electrochemically synthesized in DESs, namely ILEG, following the procedure previously reported by our group [45]. Ag-TiO₂ composites were prepared using a relatively simple method. The TiO₂ powder was dispersed in an ILEG electrolyte, and the electrochemical deposition of Ag was performed in PRC mode using a two-electrode setup based on Ag wires. In this work, we first investigated the influence of the duration of the T_{off} while maintaining the anodic and cathodic pulses at 100 mA for 100 ms. The T_{off} was gradually increased from 100 to 200 and 300 ms, to obtain the samples named Ag-TiO₂-1.1, Ag-TiO₂-1.2 and Ag-TiO₂-1.3, respectively. The PRC parameters, frequency and duty cycle are presented in Table 1. The overall process consisted of the oxidation of bulk Ag metal during the application of the anodic current (I_p⁺), followed by the T_{off}, during which the migration of the metal cations takes place, and finally, the reduction of Ag⁺ occurs, leading to the formation of Ag nuclei on the surface of TiO₂, during the application of the cathodic current (I_p⁻), as shown in Fig. 1 [35,52]. PVP was added to the ILEG electrolyte to promote Ag nucleation and minimize particle aggregation [53]. Our group has previously reported the successful decoration of MWCNTs with Ag NPs using a similar procedure [44,54,55].

The XRD patterns of the TiO₂ and Ag loaded TiO₂ composites (Ag-TiO₂-1.1, Ag-TiO₂-1.2 and Ag-TiO₂-1.3), obtained by PRC in DESs

electrolyte are shown in Fig. 2(a). The XRD revealed the presence of several diffraction peaks at $2\theta = 25.35, 37.03, 37.87, 38.80, 48.02, 53.93, 55.03, 62.75, 68.74^\circ$, unambiguously attributed to the (101), (103), (004), (112), (200), (105), (211), (204) and (116) reflections of anatase-TiO₂ with a tetragonal crystal system and lattice parameters of $a = b = 0.378 \text{ nm}, c = 0.951 \text{ nm}, \alpha = \beta = \gamma = 90^\circ$. No additional Ag-based diffraction peaks were detected, only crystalline anatase TiO₂, which could be associated with the low metal content due to the short electrodeposition time, as we will further discuss in this work [5]. The experimental XRD data were interpreted using of Rietveld refinement, employing a least-squared method to fit the theoretical profile against the experimental. To resolve a real structure, it is necessary to have a reasonable initial approximation of the unit cell dimensions or the coordinates of all atoms in the crystal structure [56–58]. By fitting the experimental data, the unit cell dimensions, mean crystallite size and lattice strain can be obtained [59,60]. In Fig. 2, for TiO₂, it is observed that the calculated data from Rietveld refinement (red line) adequately fit the experimental data across the entire angular range. The results obtained from the Rietveld refinement is summarized in Table 2.

The crystal quality is altered, as reflected in the smaller crystallite sizes for the Ag-TiO₂ composites compared to TiO₂ powder (Table 2). The decrease in the crystallite size was attributed to Ag being embedded at the grain boundaries, which prevents further grain growth [18,20]. The variation in the T_{off} between the anodic and cathodic pulses influences the crystallite size, with values of 19.9, 15.8 and 17.4 nm obtained for Ag-TiO₂-1.1, Ag-TiO₂-1.2 and Ag-TiO₂-1.3, respectively. During the T_{off}, when zero current is applied, the Ag⁺ ions can diffuse in the electrolyte and attach to the surface of TiO₂, where they will be reduced to metallic silver. The crystal structure is influenced by the balance between the rate of crystal nucleation and the growth of the already-formed crystals [35,36,61]. The optimum T_{off} was found to be 200 ms. Increasing the T_{off} to 300 ms leads to an increase in crystallite size, as a longer time promotes the growth of existing crystals. On the other hand, a shorter time of 100 ms is insufficient for Ag⁺ ion migration in the electrolyte, considering the high viscosity of DESs, which leads to

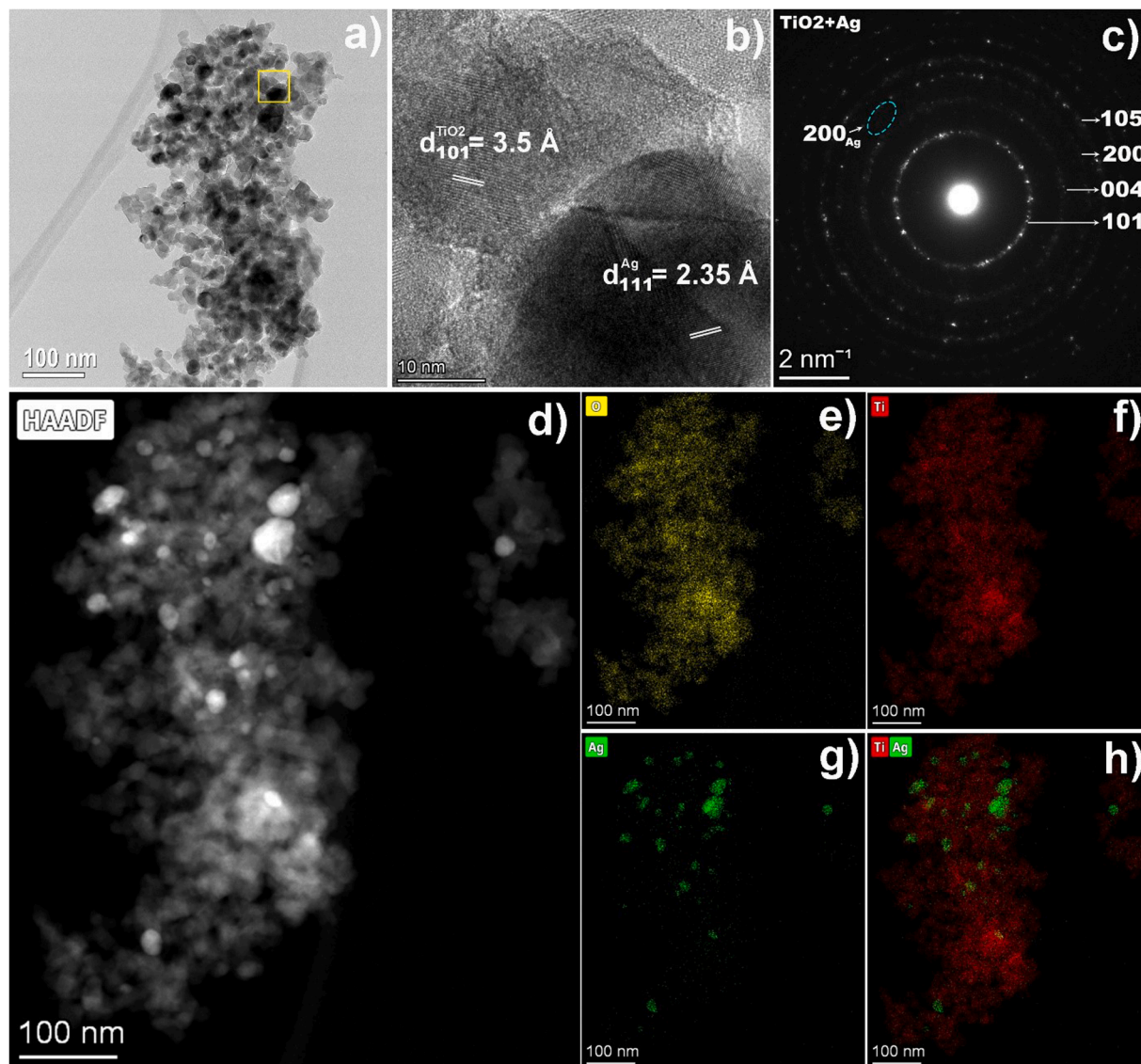


Fig. 6. (a) TEM and (b) HRTEM image of Ag-TiO₂-3 h composite, showing Ag particles on top of TiO₂; (c) SAED pattern corresponding to the TEM image (a). (d) low-magnification HAADF-STEM image and EDS mapping showing the O (e), Ti (f) and Ag (g) distribution. (h) superimposed maps of Ti and Ag.

Table 3

Surface area, pore size and pore volume for TiO₂ and Ag-TiO₂-1 h, Ag-TiO₂-3 h and Ag-TiO₂-6 h composites.

| Sample | S_{BET} (m ² g ⁻¹) | V_{micro} (cm ³ g ⁻¹) | V_{meso} (cm ³ g ⁻¹) | D (nm) |
|-------------------------|--|---|--|----------|
| TiO ₂ | 23.05 | 0.0018 | 0.0422 | 7.3 |
| Ag-TiO ₂ -1h | 16.10 | 0.0018 | 0.0320 | 7.9 |
| Ag-TiO ₂ -3h | 17.75 | 0.0023 | 0.0471 | 10.3 |
| Ag-TiO ₂ -6h | 17.75 | 0.0008 | 0.0417 | 9.7 |

* S_{BET} is the specific surface area, V_{micro} -volume of micropores ($d < 2$ nm), V_{meso} -volume of mesopores ($2 \text{ nm} < d < 50$ nm), D_p -pore diameter.

growth in the same spot. Particles with smaller crystallite size are highly desirable for a wide range of applications, including photocatalysis, sensors, and environmental remediation [16].

Building on the optimum PRC plating parameters of Ag-TiO₂-1.2, and to increase the content of Ag, the overall duration of the electrochemical process was extended from 1 h (new sample notation Ag-TiO₂-1 h) to 3 h (Ag-TiO₂-3 h) and finally to 6 h (Ag-TiO₂-6 h), as presented in Table 1. For the Ag-TiO₂ composites, the XRD patterns (Fig. 2(b)) evolve with changing electrodeposition time. No additional

Ag-based diffraction peaks were detected in the case of short electrodeposition time, Ag-TiO₂-1 h, only crystalline anatase TiO₂ observed. However, after 3 h (Ag-TiO₂-3 h), besides the characteristic TiO₂ diffraction peaks, the XRD pattern presents an additional diffraction feature at $2\theta = 44.15^\circ$, which corresponds to the (200) crystallographic plane of face-centred cubic (FCC) silver with $a = b = c = 0.407$ nm. The (111) reflection located at $2\theta = 37.93^\circ$ is not visible, as it overlaps with the anatase reflections. At 6 h (Ag-TiO₂-6 h), the specific (200) and (220) reflections of Ag appear at $2\theta = 44.15^\circ$ and 64.45° , in accordance with ICDD card No 01-1164 [62,63]. Additionally, new diffraction peaks emerge at 27.68° , 32.13° , 46.28° , 57.46° , assigned to the (110), (111), (211) and (221) reflections of cubic Ag₂O with lattice parameter of $a = 0.476$ nm according to ICDD card No 76-1393 [62-64]. Thus, the increase in electrodeposition time leads to the oxidation of silver, forming Ag₂O, since Ag NPs are prone to oxidation. The results from the Rietveld refinement are summarized in Table 2. According to the Rietveld data, despite significant changes in the final phase, the unit cell parameters of TiO₂ were not affected, preserving the values of reference TiO₂. The Ag-TiO₂-3 h sample has the smallest crystallite size (e.g. ~ 14.3 nm). However, when the Ag content was increased by extending the electrodeposition time from 3 h to 6 h, the crystallite size also

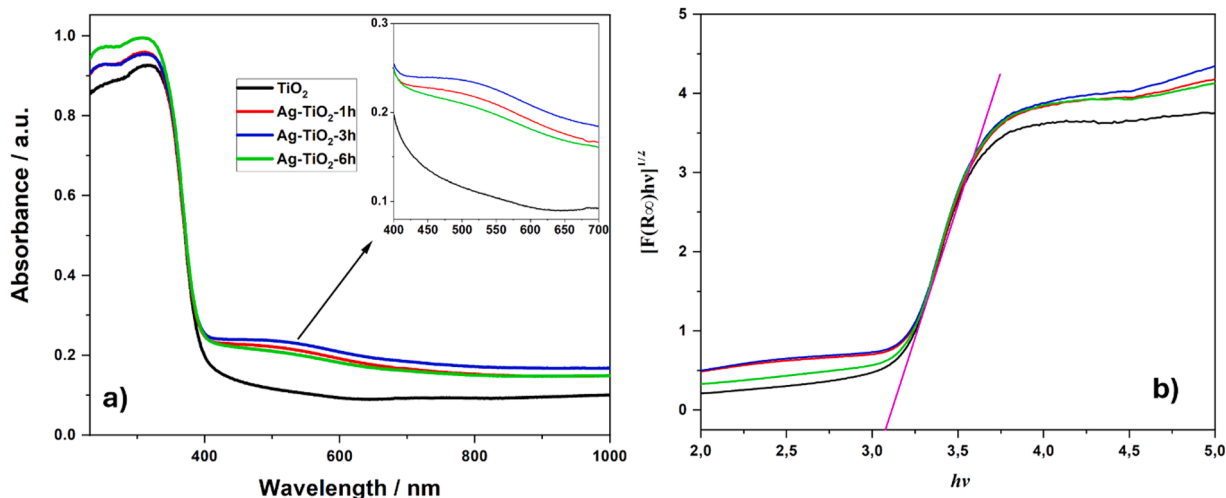


Fig. 7. a) UV-Vis diffuse reflectance spectra of TiO₂ and Ag-TiO₂ composites; b) plot of $[F(R_{\infty})hv]^{1/2}$ vs $h\nu$ for band gap calculation.

increased. Mogal et al. also reported a decrease in crystallite size for Ag NPs decorated TiO₂ [65]. The authors state that Ag incorporation at the optimum concentration hinders the crystallites growth. However, a higher Ag content, restrained at the grain boundaries, promotes grain growth and leads to larger crystallites [12,66]. Regarding the lattice strain (Table 2), it decreases in Ag-loaded samples, with a tensile strain reducing from +0.43 % to +0.06 %.

To investigate the oxidation state of the Ag-TiO₂-6 h sample, X-ray photoelectron spectroscopy (XPS) was performed on the Ti 2*p* and Ag 3*d* was region, as shown in Fig. 3.

The Ti 2*p* XPS spectrum presented in Fig. 3(a) shows components at binding energy of 464.3 and 458.5 eV, coming from 4⁺ valence state of TiO₂ (the distance between peaks is ~ 5.8 eV.) [67]. These peaks are associated with the spin-orbital splitting of Ti 2*p*_{1/2} and Ti 2*p*_{3/2}, respectively. Furthermore, in the Ag 3*d* spectrum, two peaks at binding energies of 373.45 eV and 367.45 eV are observed, corresponding to Ag 3*d*_{3/2} and Ag 3*d*_{5/2}, respectively. The peak at 367.45 eV (3*d*_{5/2}) is lower than the peak of metallic Ag (368.2 eV for Ag⁰) and closer to those of silver oxides (367.6 eV for AgO and 367.9 eV for Ag₂O) [68,69], thus confirming the XRD findings.

The SEM analysis of TiO₂ and Ag-TiO₂ composites is presented in Fig. 4, offering a general view of the NPs. The SEM images indicate that the morphology of the samples is preserved after Ag-loading of the TiO₂. Spherical particles with nanometric sizes (~10–20 nm) are observed. The presence of Ag was confirmed by EDX analysis. As the overall duration of the electrochemical process increased, the Ag content in the powder increases from 0.3 wt. % for Ag-TiO₂-1 h to 0.6 wt. % for Ag-TiO₂-3 h and 2.6 wt. %, for Ag-TiO₂-6 h (Fig. S1 and Table S1 in supplementary material). Apart from Ag, Ti and O elements were identified in an atomic ratio of approximately 1:2.

While SEM imaging provides a good understanding of NPs morphology and size, TEM is a more suitable technique for studying nanoobjects, as its higher resolution plays a crucial role. The S/TEM images, presented in Fig. 5, show TiO₂ NPs with high crystallinity and spherical morphology. The TEM measurements confirmed the average size determined by XRD (~27 nm). In the HRTEM image presented in Fig. 5(b), the (111) planes corresponding to d_{TiO_2} =3.5 Å were identified. STEM image (Fig. 5(a)) at low magnification showcases the homogeneity of the TiO₂ NPs obtained electrochemically in DES solvent. The anatase phase of the TiO₂ NPs was confirmed using Fast Fourier Transform (FFT, Fig. 5(f)), corresponding to the High-Angle Annular Dark Field – STEM (HAADF-STEM) image (Fig. 5(c)) at atomic resolution, where a NP along the [111] zone axis was identified. The zoomed-in area (Fig. 5(d)) extracted from Fig. 5(c) shows the exact position of Ti and O atomic columns, verified by the simulated HAADF-STEM image

(Fig. 5(e)) using the atomic model of anatase from Fig. 5(g).

The TEM images of the Ag-TiO₂-3 h composite reveal spherical Ag NPs (darker particles) with diameters of 19.5 ± 10 nm, distributed on the agglomerated TiO₂ NPs (Fig. 6(a)). The Ag NPs predominantly range between 10–35 nm, with the largest reaching 50 nm. TEM investigations did not show individual Ag NPs. The distribution of Ag NPs on TiO₂ is influenced by the PRC plating mechanism, see Fig. 1. During the electrodeposition process, the sacrificial bulk Ag metal anode dissolves, forming Ag⁺ ions that migrate and attach to the TiO₂ NPs during the T_{off} period. These ions subsequently reduce to metallic Ag(0) on the surface of TiO₂ upon the application of the cathodic current. This process facilitates the formation of Ag nuclei across the TiO₂ surface.

The HRTEM image in Fig. 6(b) shows Ag NPs (darker particles), marked with d_{111} =2.35 Å, on top of TiO₂ NPs, with d_{101} =3.5 Å. The SAED pattern in Fig. 6(c) confirms the anatase structure of TiO₂ NPs as main part of the diffraction pattern, with faint spots (cyan-dotted oval) corresponding to (200) planes of FCC structure of metallic Ag. Fig. 6(d) presents a low-magnification HAADF-STEM image of the Ag-TiO₂-3 h composite, where the mass-thickness contrast reveals the precise position of Ag NPs. The mass-thickness contrast can be directly interpreted, being based on atomic number (Z) of the elements and thickness, bright/darker areas correspond to heavy/light elements. The EDS elemental mapping in Fig. 6(e) and (f) illustrates the homogeneous distribution of O and Ti elements within the TiO₂ agglomerates, while Fig. 6(g) shows the presence of Ag. The superimposed EDS maps in Fig. 6(h) show how Ag NPs are dispersed between TiO₂ NPs.

The specific surface area of the TiO₂ powder and Ag-TiO₂ composites presented in Table 3 was extracted from the N₂ adsorption-desorption isotherms. There is a slight decrease in the surface area when Ag NPs are formed on the surface of TiO₂. When the overall duration of the electrochemical process is increased from 1 h to 3 h and 6 h, there is no significant variation in the specific surface area, with values remaining around 17 m² g⁻¹. Saravanan et al. reported a significant decrease in the surface area upon silver addition, which was attributed to the aggregation of TiO₂ crystallite during the preparation of the material [28]. Interestingly, among the different synthesized samples, Ag-TiO₂-3 h exhibits the largest volume of micro- and mesopores, with a pore diameter of 10.3 nm.

Fig. 7a shows the diffuse reflectance spectra (DRS) of TiO₂ and Ag-TiO₂ composites. The absorption edge at ~400 nm is attributed to electron transfer from the valence band to the conduction band of TiO₂. As presented in Fig. 7a, the DRS spectra of the Ag-loaded samples differ from those of pure TiO₂. The absorption of the composite samples slightly increases in the visible light region, from 400 to 650 nm, with the Ag-TiO₂-3 h sample exhibiting the highest absorption in this region.

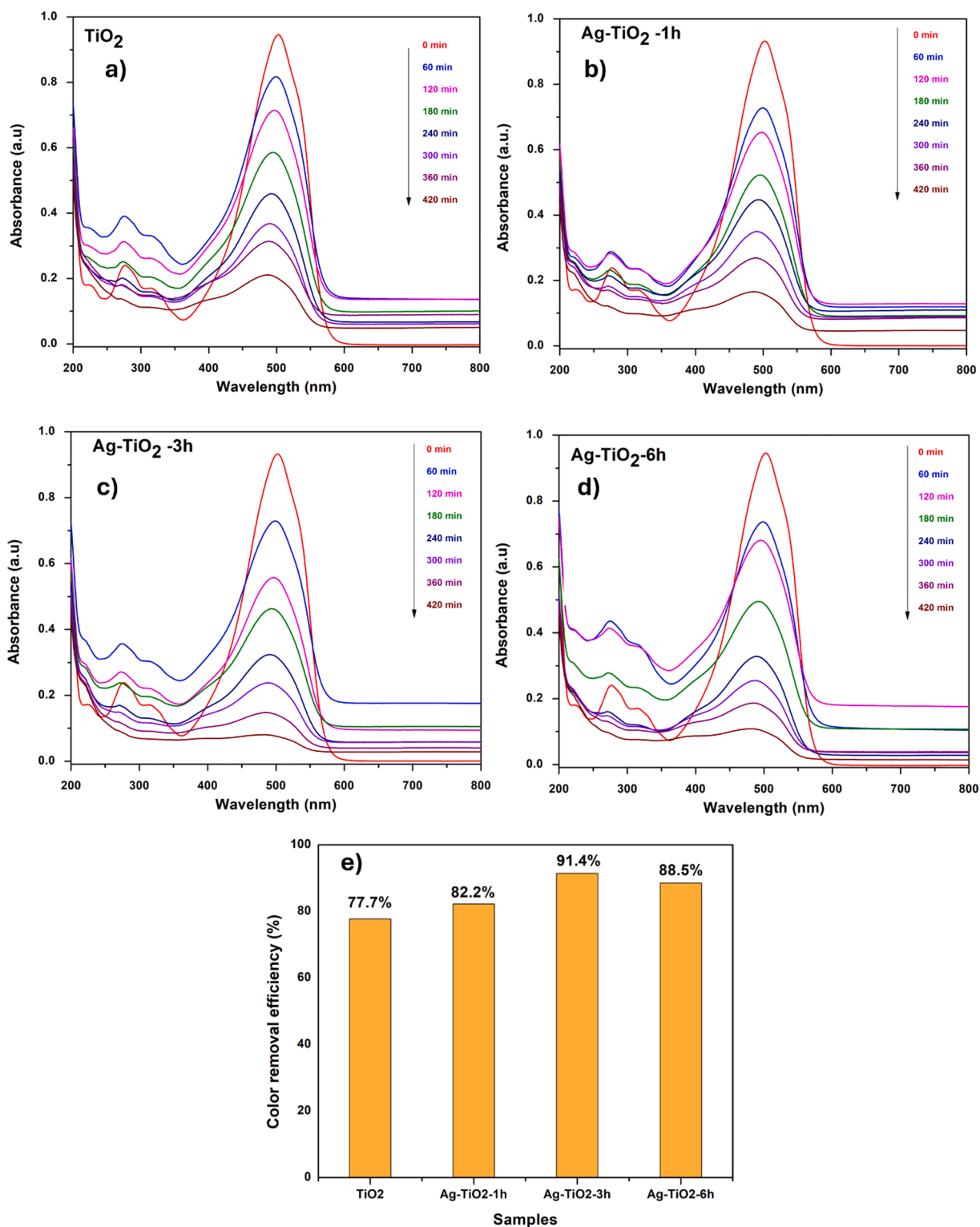


Fig. 8. UV-Vis absorption spectra of MO dye solution during photocatalytic degradation under UV in the presence of (a) pure TiO₂, (b) Ag-TiO₂-1 h, (c) Ag-TiO₂-3 h and (d) Ag-TiO₂-6 h; (e) Bar diagram of colour removal efficiency (%) of MO for pure TiO₂ and the composites Ag-TiO₂-1 h, Ag-TiO₂-3 h and Ag-TiO₂-6 h.

The observed broadening of the absorbance band, associated with the LSPR of Ag NPs on the surface of a semiconductor (generally located around 400 nm), could be the effect of Ag NPs interaction with TiO₂ [20, 70,71]. Furthermore, an increase in Ag concentration (2.6 wt % for Ag-TiO₂-6 h) does not improve absorption in the visible region, the values obtained being similar to those observed at shorter electrochemical synthesis time, Ag-TiO₂-1 h. This phenomenon could be

associated with the formation of Ag₂O oxide at longer electrodeposition times, 6 h, as evidenced by XRD analysis (see Fig. 2.) Wu et al. reported a strong damping of the LSPR of Ag NPs when silver oxide, Ag₂O, is produced [72]. In another work, Mogal *et al.*, observed that upon increasing the silver content on Ag-TiO₂ composites, the visible absorption band disappeared on higher silver loaded samples [65].

The band gap energy (E_g) of TiO₂ and Ag-TiO₂ composites was

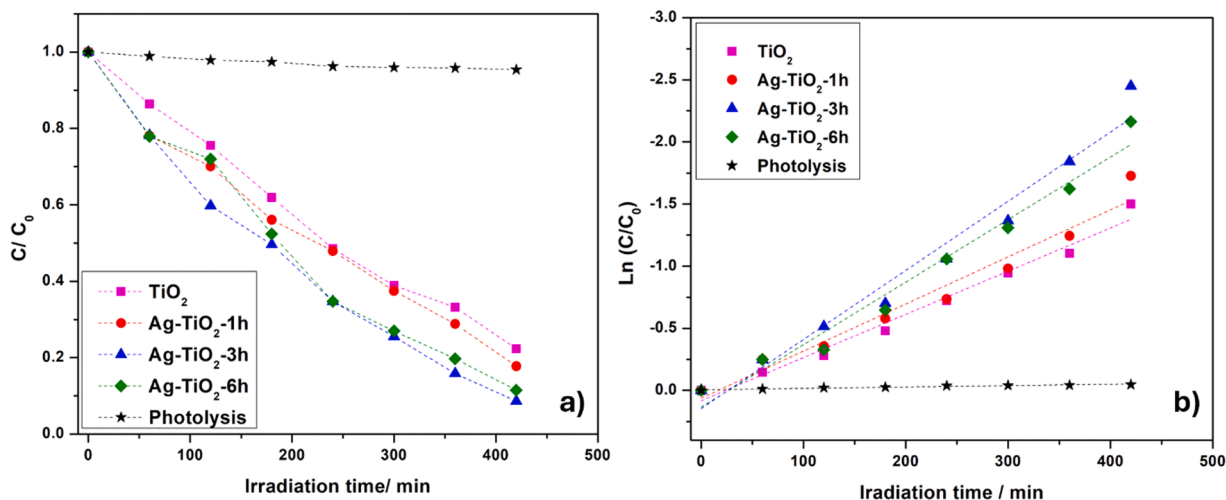


Fig. 9. (a) Residual MO dye after different irradiation times under UV in the presence of pure TiO_2 and the composites $Ag-TiO_2-1$ h, $Ag-TiO_2-3$ h and $Ag-TiO_2-6$ h; and (b) linear plots of $\ln(C/C_0)$ versus the irradiation time of MO dye.

determined from the DRS spectra by extrapolating the linear region of the plot of $[F(R_\infty)h\nu]^{1/2}$ vs $h\nu$, according to the Kubelka-Munk theory under the assumption of an interband direct transition [12,73], where $F(R_\infty)$ is the Kubelka-Munk function, R_∞ is the absolute reflectance of sample, $h\nu$ is the photon energy and E_g the band gap energy (Fig. 7b). No significant change in the E_g is observed, with the value for TiO_2 was slightly reduced from 3.13 to 3.10, 3.07, and 3.12 eV for $Ag-TiO_2$ composites at 1 h, 3 h, and 6 h, respectively. The observed band gaps are consistent with the ones reported for anatase TiO_2 and Ag-loaded composites [12,17,18,66,74–77]. The band gap of the $Ag-TiO_2$ composite is known to be significantly influenced by the silver content incorporated into the composite, exhibiting values from 3.3 to 2.67 eV at 3 % and 10 % Ag loading [25,77]. In the current study, the Ag concentration was limited to 2.6 wt % and, as a result, no significant band gap variation was detected.

3.2. Photocatalytic experiments

The photocatalytic activity of TiO_2 and $Ag-TiO_2$ composites was estimated by the degradation of MO dye (10 mg/mL) under UV and visible light illumination. The experiments were performed at the optimum pH value of 3 (see Fig. S2). Under acidic conditions, the surface of the TiO_2 is positively charged, facilitating the adsorption of the dye and therefore enhancing the photodegradation efficiency [78]. The concentration of the powdered catalyst in the solution was fixed at 1 g/L, and the samples were evaluated at the initial moment and every hour for 6–7 h of irradiation. The effect of the photocatalytic activity under UV is presented in Fig. 8, while for visible light illumination in Fig. 10. Under UV, pure TiO_2 exhibits a degradation efficiency of 77.7 % while the composites exhibited higher efficiencies: 82.2, 91.4 and 88.5 % for $Ag-TiO_2-1$ h, $Ag-TiO_2-3$ h and $Ag-TiO_2-6$ h, respectively (Fig. 8(e)). Additionally, a relatively high photodegradation efficiency of around 60.2 % was observed for $Ag-TiO_2-3$ h composite after visible light illumination, compared to 32.3 % for pure the TiO_2 sample, showcasing the benefits of Ag-loading (see Fig. 10(e)). The photocatalytic activity under visible light is improved by Ag incorporation, even for short electrodeposition time, $Ag-TiO_2-1$ h exhibiting a degradation efficiency of 41.5 % while $Ag-TiO_2-6$ h showed 55.2 % efficiency (see Fig. 10(e)). $Ag-TiO_2$ composites significantly outperform pure TiO_2 in terms of photodegradation efficiency under both UV and visible light. The addition of Ag is beneficial for the photodegradation process, as it acts as an electron trap, transferring electrons to the TiO_2 conduction band and subsequently to oxygen, generating superoxide radicals. Simultaneously, the holes in the valence band react with water, forming

hydroxyl radicals that drive the photocatalysis of pollutants. Additionally, Ag loading induces a surface plasmon resonance effect, as demonstrated by the DRS analysis (Fig. 7), boosting light absorption in the visible region, further improving TiO_2 's photodegradation efficiency [16–18].

The Langmuir-Hinshelwood (LH) model was used to determine the kinetic rate constant of the photocatalytic reaction, using the following equation:

$$r = -\frac{dC}{dt} = \frac{kK_{ad}C}{1 + K_{ad}C} \quad (3)$$

where r - reaction rate, C - is the dye concentration within a time interval t , k - is the reaction rate constant and K_{ad} - adsorption constant accounting the attachment of the dye molecules on the photocatalyst surface. Considering that the dye concentration is low, the equation is simplified to [79]:

$$-\ln \frac{C}{C_0} = kK_{ad}t = k_{app}t \quad (4)$$

where $k_{app} = kK_{ad}$ the pseudo-first-order reaction rate constant, and C_0 the initial dye concentration

In Fig. 9(a) and Fig. 11(a), the decolorization of the MO dye in the presence of TiO_2 and $Ag-TiO_2$ composites at different illumination times, under UV and visible light conditions, is presented. It can be observed that the concentration of the MO dye decreases as a function of irradiation time. In contrast, the degradation of the MO dye in the absence of the nanopowder is considerably low (marked as the photolysis process on the plots).

The pseudo-first-order reaction rate constant of the photocatalytic reaction was determined from the slope of the linear fit of $-\ln \frac{C}{C_0}$ vs time (Eq. (4)), as shown in Fig. 9(b) and Fig. 11(b) for UV and visible illumination. Among all samples, $Ag-TiO_2-3$ h presents the fastest decay rates, $5.56 \times 10^{-3} \text{ min}^{-1}$ and $2.14 \times 10^{-3} \text{ min}^{-1}$ for degradation under UV (Table 4) and visible illumination (Table 5), respectively. Clearly, the addition of Ag, improved the photocatalytic activity under both UV and visible light. The pseudo first-order reaction rate constant is around two-fold higher for $Ag-TiO_2-3$ h ($k_{app} = 2.14 \times 10^{-3} \text{ min}^{-1}$) than for TiO_2 samples ($k_{app} = 1.03 \times 10^{-3} \text{ min}^{-1}$) under visible light.

Among the different samples, $Ag-TiO_2-3$ h is a more efficient photocatalyst under both UV and visible light illumination compared to pure TiO_2 and $Ag-TiO_2$ samples with higher Ag content, namely $Ag-TiO_2-6$ h. The degradation of MO was slightly lower for both UV and visible illumination when the electrodeposition time increasing from 3

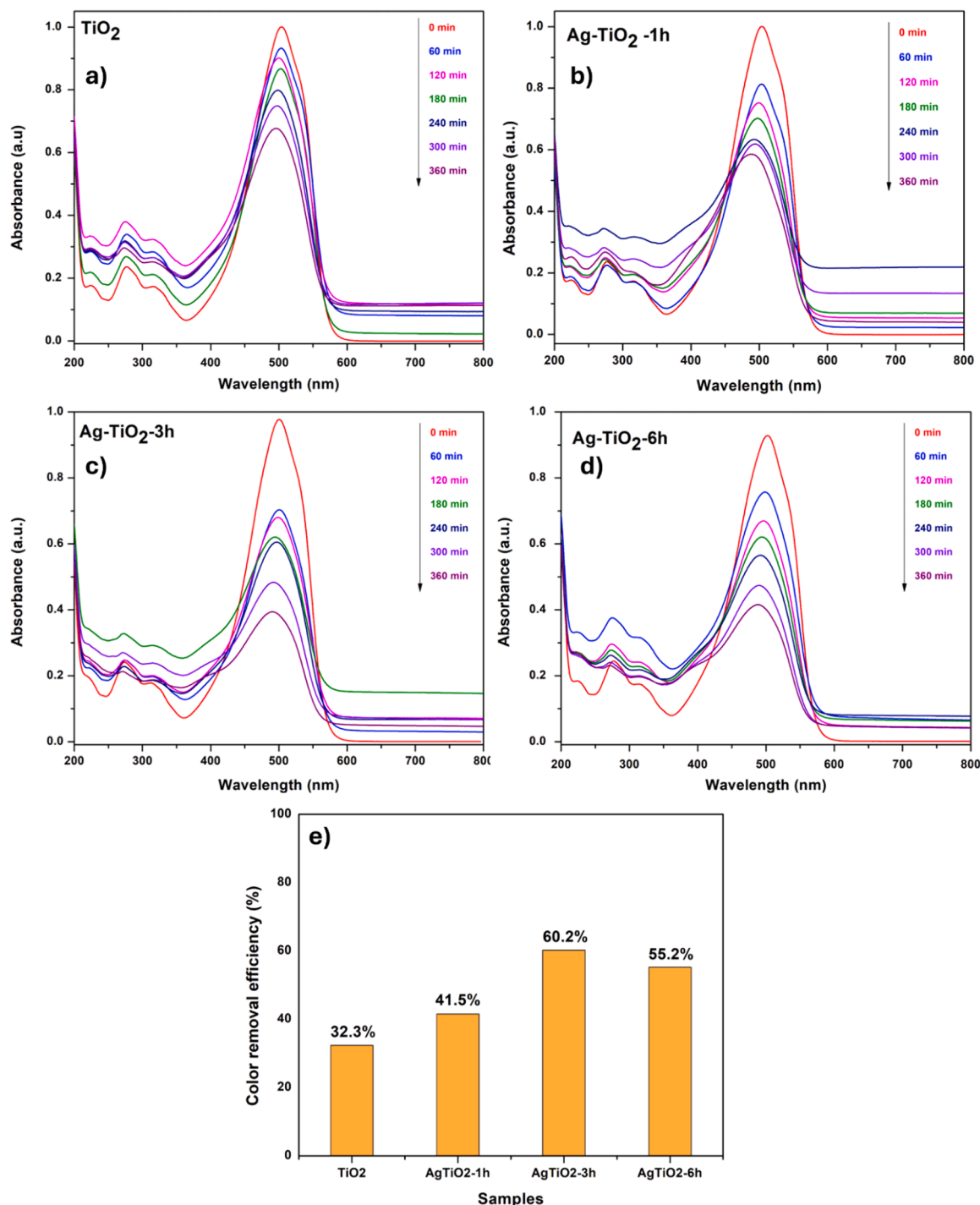


Fig. 10. UV-Vis absorption spectra of MO dye solution during photocatalytic degradation under visible light in the presence of (a) pure TiO₂, (b) Ag-TiO₂-1 h, (c) Ag-TiO₂-3 h and (d) Ag-TiO₂-6 h; (e) Bar diagram of colour removal efficiency (%) of MO for pure TiO₂ and the composites Ag-TiO₂-1 h, Ag-TiO₂-3 h and Ag-TiO₂-6 h.

to 6 h, which led to an increase in Ag content from 0.6 wt. % to 2.6 wt. %. The decrease in the photocatalytic activity could be associated with the increase in Ag concentration, resulting in the agglomeration of Ag NPs. The formation of the Ag₂O crystalline phase has been reported to improve the photocatalytic activity [79,80], in our case the agglomeration of Ag NPs has a greater impact than the presence of Ag₂O. Similar to other studies, the intermediate silver content and larger specific surface area are the key characteristics of the photodegradation efficiency. For instance, several reports showed that increasing the Ag content above a certain threshold decreases the photocatalytic activity [65,81–83]. Rahmawati and co-workers reported a similar effect of Ag

concentration on the photodegradation of methylene blue dye under visible light. Among the different samples prepared - 0.5 % Ag-TiO₂, 1 % Ag-TiO₂, 3 % Ag-TiO₂ and 6 % Ag-TiO₂ - the optimal catalytic activity was demonstrated for the 3 % Ag-TiO₂ particles [81]. The authors associated the increased photocatalytic activity of 3 % Ag-TiO₂ with the high surface area, while a higher concentration of Ag, generates the agglomeration of Ag NPs into larger clusters on the TiO₂ surface, limiting the available sites for surface reactions, hindering light absorption, and reducing the adsorption of reactant molecules by TiO₂. In addition, high, Ag content can serve as recombination centres, leading to a reduction in the photocatalytic activity of TiO₂ [77,79,84].

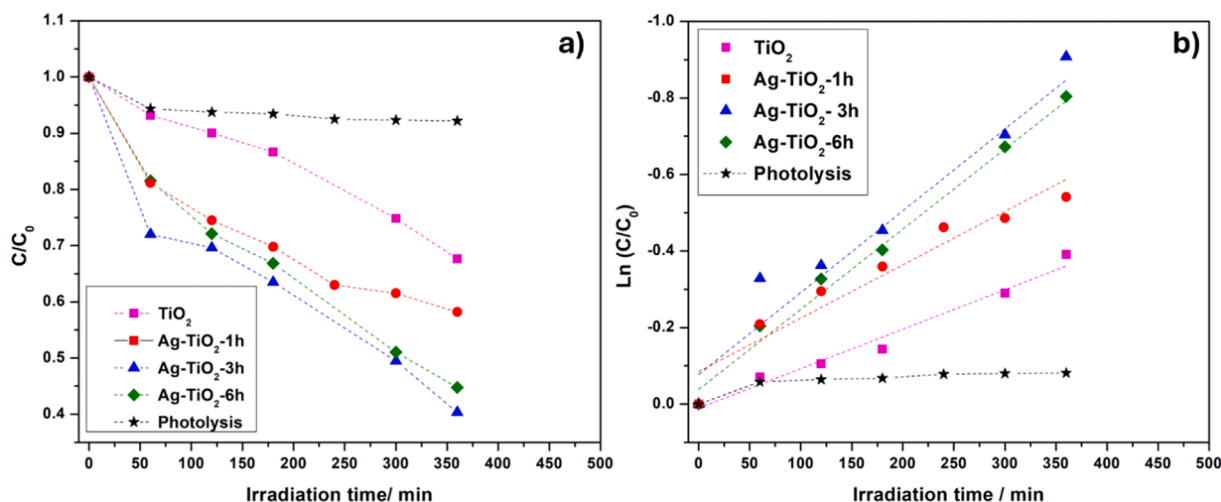


Fig. 11. (a) Residual MO dye after different irradiation times under visible light in the presence of pure TiO_2 and the composites $Ag-TiO_2-1h$, $Ag-TiO_2-3h$ and $Ag-TiO_2-6h$; and (b) linear plots of $\ln(C/C_0)$ versus irradiation time for the degradation of MO dye.

Table 4

k_{app} values for pure TiO_2 and the $AgTiO_2-1h$, $AgTiO_2-3h$ and $AgTiO_2-6h$ composited under UV light.

| Photocatalyst type | $k_{app} (\times 10^{-3}), \text{min}^{-1}$ | R^2 |
|--------------------|---|-------|
| TiO_2 | 3.48 | 0.978 |
| $Ag-TiO_2-1h$ | 3.79 | 0.959 |
| $Ag-TiO_2-3h$ | 5.56 | 0.962 |
| $Ag-TiO_2-6h$ | 5.03 | 0.969 |

Table 5

k_{app} values for pure TiO_2 and the $AgTiO_2-1h$, $AgTiO_2-3h$ and $AgTiO_2-6h$ composites under visible light illumination.

| Photocatalyst type | $k_{app} (\times 10^{-3}), \text{min}^{-1}$ | R^2 |
|--------------------|---|-------|
| TiO_2 | 1.03 | 0.971 |
| $Ag-TiO_2-1h$ | 1.40 | 0.913 |
| $Ag-TiO_2-3h$ | 2.14 | 0.908 |
| $Ag-TiO_2-6h$ | 2.09 | 0.982 |

A table comparing the photodegradation efficiency of various photocatalysts towards the degradation of MO dye is presented in the supplementary section (Table S2). The $Ag-TiO_2$ NPs synthesised via PRC electrodeposition exhibited a high MO degradation efficiency of 91.4 % under a low-power UV lamp (6 W, $\lambda = 365$ nm). This performance is comparable to other studies reported in the literature that utilized significantly higher power sources (e.g. 100 W or 500 W UV lamps), yet it achieves substantial pollutant removal with a significantly lower energy consumption, 42 Wh. Moreover, the electrochemical synthesis method used in this study offers a scalable and cost-effective alternative to conventional synthesis routes, making it well-suited for large-scale environmental applications, while the use of DESs electrolytes enhances sustainability [34,41].

Furthermore, to evaluate the stability of the photocatalyst, the $Ag-TiO_2-3h$ composite was reused in a second photodegradation test. After the first cycle of photodegradation, the powder was cleaned, dried at 60 °C and recycled to photodegradation analysis under UV conditions. The efficiency of the recovered catalyst decreased from 91.4 to 80.2 %, as shown in Fig. 12(e). The XRD analysis did not show significant changes on the structure of the nanopowder (Fig. 12(c)); however, the SEM-EDX measurements indicated incomplete removal of the organic dye, which adhered to the surface of the composite and could reduce its photocatalytic activity. The morphology of the sample was slightly altered,

with fibrous structures visible (indicated by arrows in Fig. 12(a)), which are attributed to the dye residue. The EDX mapping (Fig. 12(b)) clearly identified N and C elements, which are part of the organic dye composition. The silver content in the composites remained unchanged after reutilization.

3.3. Antimicrobial activity

Pulse plating of Ag onto the surface of TiO_2 NPs was effective, demonstrating that this method can serve as an alternative approach to enhance the photocatalytic activity of TiO_2 under both UV and sunlight irradiation. Considering that the optimum amount of Ag-loading to improve photocatalytic activity is 0.6 wt. %, which was achieved after 3 h of electrodeposition, namely $Ag-TiO_2-3h$ sample, its antimicrobial activity was evaluated against Gram-negative and Gram-positive strains, specifically *E. coli* and *B. subtilis var spizizenii*, respectively.

The result of the antimicrobial activity is expressed as the zone of inhibition (IZ, mm), represented by the clear zone around the samples, as shown in Fig. 14. From the analysis of the inhibition zones, TiO_2 nanopowder exhibits good antibacterial activity against Gram-negative strains, specifically *E. coli*, with a microbial inhibition zone of 16.5 ± 0.94 mm. However, the antibacterial effect against *B. subtilis var spizizenii*, a Gram-positive strain is limited, with the NPs exhibit an inhibition zone of 5 ± 0.12 mm. In comparison to TiO_2 nanopowder, the activity of the $Ag-TiO_2$ composite was significantly higher against *B. subtilis var spizizenii*. The inhibition zone increased from 5 ± 0.12 mm to 23 ± 0.05 mm with the incorporation of Ag. The antimicrobial effect against *E. coli* was also enhanced with the incorporation of Ag, with the inhibition zone increasing from 16.5 ± 0.94 mm for TiO_2 to 18.5 ± 0.86 mm for the $Ag-TiO_2$ composite. (Fig. 13, Fig. 14)

Our results are consistent with previous reports in the literature. Landage et al. reported an inhibition zone of 14 mm for TiO_2 NPs against *E. coli* and 9 mm for *B. subtilis* [85]. The authors observed that Gram-negative bacteria are more sensitive to TiO_2 NPs compared to Gram-positive strains. Yuan and co-authors reported a microbial inhibition zone of 27 mm against *E. coli* and 21.3 mm against *B. subtilis* for a 1 % $Ag-TiO_2$ composite, while for TiO_2 NPs, the inhibition zone was found to be 16 and 15.2 mm, respectively [86]. The antimicrobial activity of TiO_2 NPs has been linked to the reactive oxygen species (ROS), such as $\cdot OH$, $\cdot O_2$, and $\cdot OH_2$, which affect bacterial cells. The formation of these ROS radicals leads to cell death through various mechanisms, including damage to the cell wall, cell membrane, DNA, etc. [87]. The incorporation of Ag NPs clearly increased the antibacterial properties, especially against Gram-positive species. The antimicrobial properties of Ag NPs

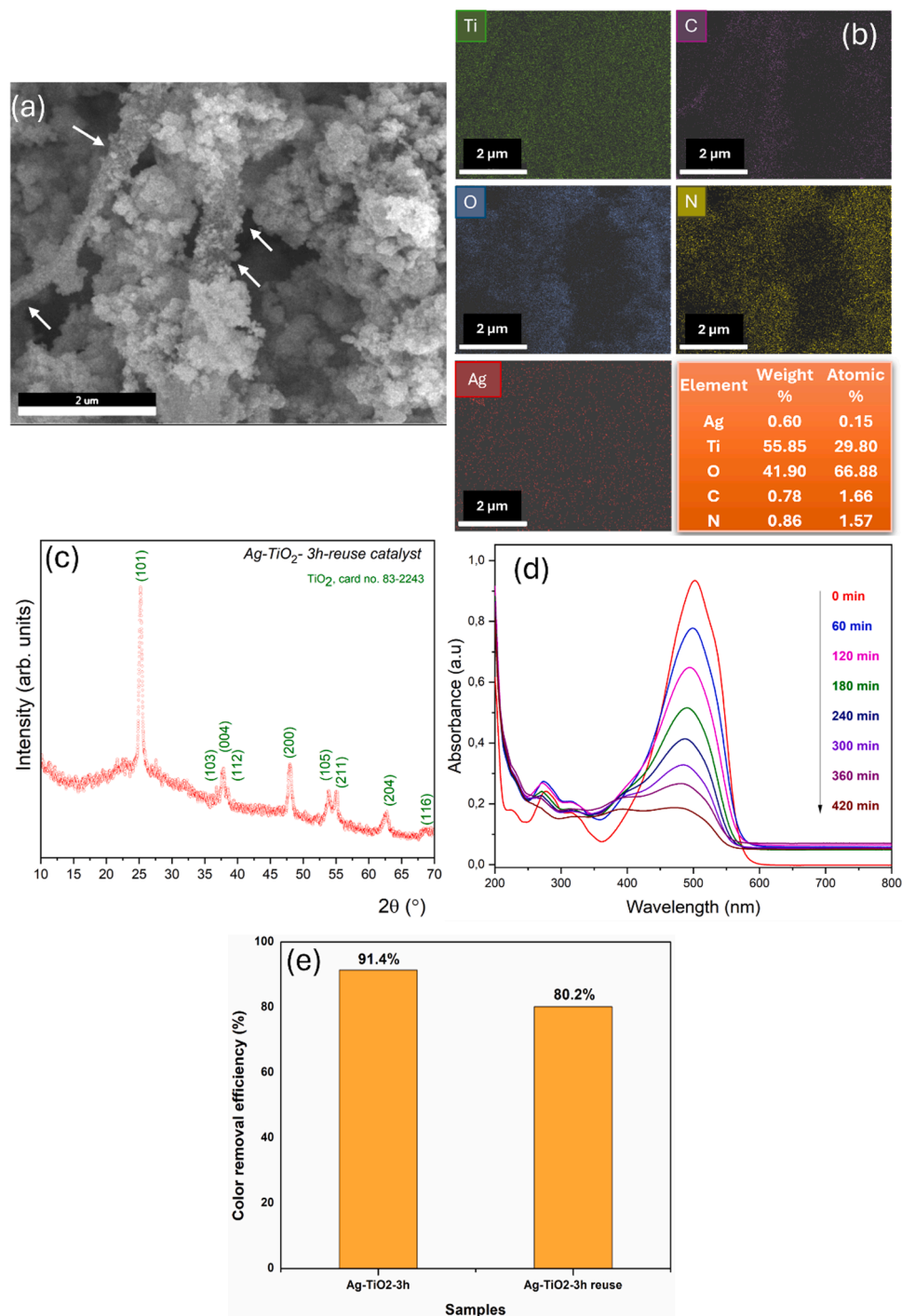


Fig. 12. (a) SEM, (b) EDX elemental mapping and (c) XRD pattern of the recycled Ag-TiO₂-3 h catalyst; (d) UV-Vis absorption spectra of MO dye using the Ag-TiO₂-3 h recycled composite and (e) colour removal efficiency after 420 min of exposure to UV light of the as-prepared and recycled Ag-TiO₂-3 h composite.

are well known; however, the mechanism is not fully understood. First, Ag NPs can cause membrane damage to bacterial cells by attaching to the sulphur groups present on the membrane. Second, Ag⁺ can be released from the NPs, damaging DNA/RNA and respiratory enzyme activity [88]. The difference in antimicrobial activity against Gram-negative and Gram-positive strains depends on the structure of the bacterial cell wall, which is thicker in Gram-positive strains compared to Gram-negative bacteria [89]. Furthermore, the obtained nanopowder can be distributed on different surfaces and used in several industries for antibacterial effect, such as leather and footwear [90].

3.4. Mechanism of catalyst analysis

To understand the photocatalytic mechanisms, free radical capture experiments were conducted on the best-performing sample, Ag-TiO₂-3 h, to explore the main species involved in the degradation of MO. Ethylenediaminetetraacetic acid disodium (Na₂EDTA), isopropanol (IPA) and benzoquinone (BQ) were used as capture agents for holes (h^+), hydroxyl radical ($\bullet OH$), and superoxide radical ($\bullet O_2^-$) respectively [91, 92]. The degradation efficiency under UV light in the absence of scavenger was 91.4 % and it dropped to 61.2 %, 57.7 % and 11.2 % upon the addition of/ IPA, Na₂EDTA and BQ, respectively. This suggests that all

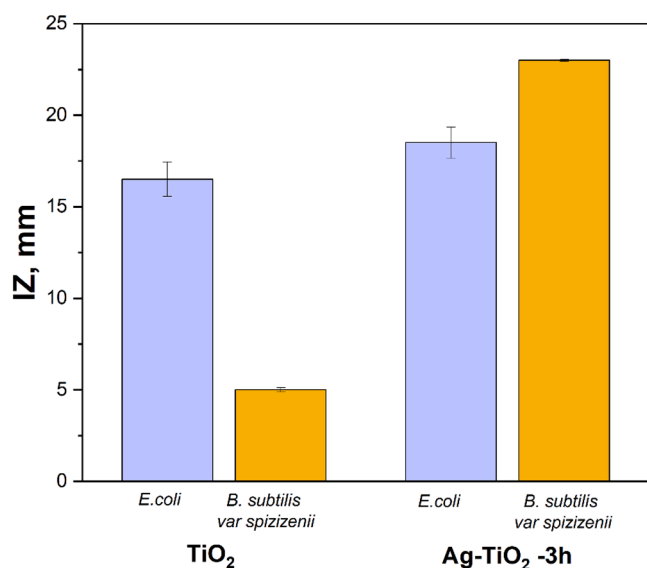


Fig. 13. Antimicrobial activity of TiO₂ and Ag-TiO₂-3 h composite against *E. coli* and *B. subtilis var spizizenii*. (**IZ – hallow zone around sample where the bacterial growth is diminished but not totally inhibited).

three species, h^+ , $\bullet OH$, and $\bullet O_2^-$ are involved in the photodegradation of MO (see Fig. S3). BQ strongly inhibited the photodegradation process, suggesting that $\bullet O_2^-$ is the main radical involved in the degradation of the organic dye.

Fig. 14 depicts the photodegradation and antibacterial behaviour of Ag-TiO₂ composites. The CB and VB edge for the best-performing sample, Ag-TiO₂-3 h composite, were determined based on the band gap energy obtained from Fig. 7b, using the following formulas:

$$E_{CB} = X - E_e - \frac{E_g}{2}$$

$$E_{VB} = E_{CB} + E_g$$

where E_{CB} and E_{VB} are the CB and VB edge level potential, E_g is the band gap (3.07 eV), E_e is the energy of free electrons (~ 4.5 eV) and X is the electronegativity of the semiconductor (for TiO₂ = 5.80 eV, and for Ag-TiO₂-3 h ~ 5.792 eV, determined by considering the sample

composition) [93,94]. The CB and VB edge level potential were calculated -0.23 eV and 2.83 eV, respectively.

Under light irradiation, photon absorption leads to electronic excitation from the valence band (VB) of the semiconductor towards the conduction band (CB), generating pairs of electrons (e^-) and holes (h^+). The photogenerated electron-hole pairs are involved in oxidation/reduction reaction with the pollutant adsorbed on the TiO₂ surface, namely MO. The h^+ react with water molecules (H₂O) to form hydroxyl radicals ($\bullet OH$), while the electrons react with molecular oxygen (O₂) to form superoxide radicals ($\bullet O_2^-$). The resulting reactive oxygen species (ROS) then react with the pollutants (MO) or microorganisms present on the semiconductor surface, decomposing them. The loading of TiO₂ with Ag NPs improves the photodegradation activity in two ways: retarding the electron-hole recombination and extending the absorption into the visible light spectrum [18,67]. The electrons in the conduction band (CB) of TiO₂ can be transported to Ag NPs, where they will react with oxygen, forming superoxide radicals ($\bullet O_2^-$). The LSPR effect of Ag NPs, under visible light, promotes electrons from the surface of Ag into the CB band of TiO₂, enhancing the photocatalytic activity towards the formation of hydroxyl radicals [95,96]. The production of ROS by the composite disrupts the integrity of bacterial cell membranes, causing the leakage of intracellular components, which consequently leads to cell death. Furthermore, Ag NPs possess antibacterial properties with or without light activation, as they can damage the bacterial membrane, and Ag⁺ can be released from Ag NPs, broadening the application of the composite in the biomedical field [18].

4. Conclusions

In this work, an easy route to electrochemically prepare Ag-TiO₂ composites using PRC electrodeposition method from DESs electrolyte is reported. Various PRC parameters were investigated, including T_{off} values of 100, 200 and 300 ms. XRD analysis revealed the lowest crystallite size at a T_{off} of 200 ms, which was selected as the optimal parameter. The electrodeposition time was then varied from 1 h (Ag-TiO₂-1 h) to 3 h (Ag-TiO₂-3 h) and 6 h (Ag-TiO₂-6 h) to further increase the Ag content. TEM analysis showed that Ag NPs were attached to the surface of anatase TiO₂ NPs, with an average size of 19.5 ± 10 nm. DRS revealed a broad absorption peak between 400 and 650 nm, corresponding to the LSPR of Ag NPs, which decreased at longer electrodeposition times. The photocatalytic activity of TiO₂ NPs and Ag-TiO₂ composite was tested towards the degradation of MO dye under UV (6 W

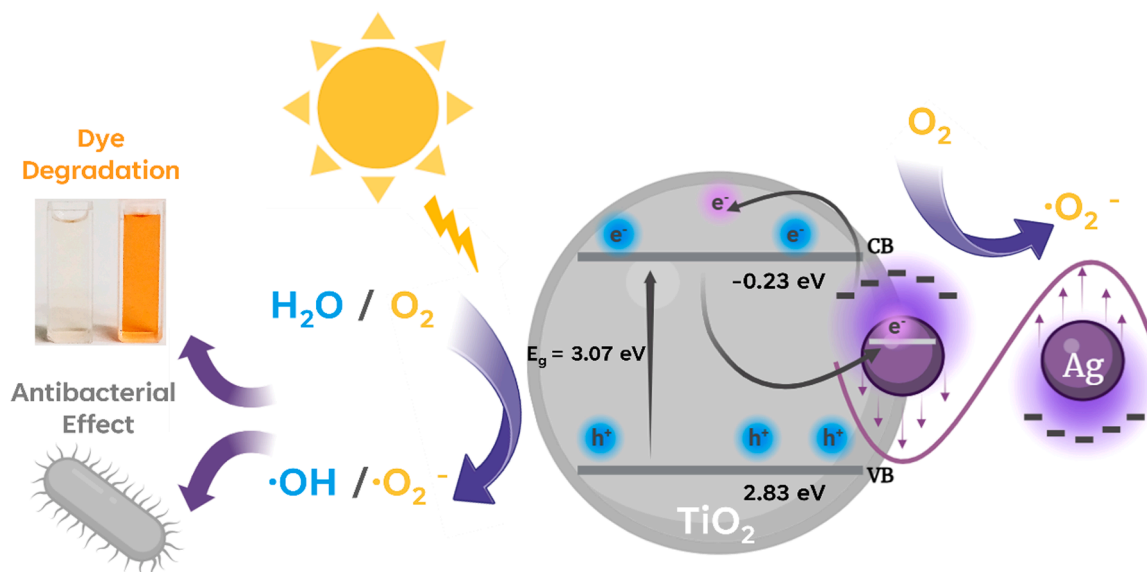


Fig. 14. Photocatalytic activity and antibacterial effect of Ag-TiO₂ composite.

lamp) and visible light illumination (solar simulator, 100 mW/cm²). The incorporation of Ag clearly increases the photocatalytic efficiency, with the Ag-TiO₂-3 h composite achieving nearly double the efficiency of pure TiO₂ nanopowder under visible light illumination, with low power consumption. Reusability tests indicated a slight decrease in the photodegradation efficiency, attributed to dye adsorption on the surface. The mechanism of MO dye degradation was explored using various scavengers, revealing that superoxide radicals ($\bullet\text{O}_2^-$) play a dominant role. The antimicrobial activity of TiO₂ and Ag-TiO₂-3 h composite was assessed against Gram-positive (*B. subtilis*) and Gram-negative (*E. coli*) species. Clearly, the incorporation of Ag improves the antibacterial activity, which is significantly higher against Gram-positive strains.

Therefore, due to its excellent photocatalytic and antibacterial activities, Ag-TiO₂ composite could be used in environmental remediation for the decomposition of organic pollutants and as effective biocide to eliminate Gram-negative and Gram-positive bacteria. Future work should focus on scaling up the production of Ag-TiO₂ composite while exploring its integration with other sustainable sources, such as carbon derived from residual waste, to further enhance its properties.

CRediT authorship contribution statement

Ionela-Cristina Petcu: Investigation, Formal analysis, Data curation. **Raluca Negrea:** Formal analysis, Data curation. **Ana T.S.C. Brandão:** Writing – review & editing, Investigation, Formal analysis, Data curation. **Cosmin Romanitan:** Writing – review & editing, Investigation, Formal analysis, Data curation. **Oana Brincoveanu:** Investigation, Formal analysis. **Nikolay Djourellov:** Investigation, Formal analysis. **Iuliana Mihalache:** Investigation, Formal analysis. **L. Monica Veca:** Investigation, Formal analysis, Data curation. **Gabriela Iso-pencu:** Methodology, Investigation, Formal analysis, Data curation. **Carlos M. Pereira:** Writing – review & editing, Methodology, Formal analysis. **Liana Anicai:** Writing – review & editing, Validation, Supervision, Methodology, Conceptualization. **Cristina Busuic:** Writing – review & editing, Methodology, Investigation, Conceptualization. **Sabrina State (Rosoiu):** Writing – review & editing, Writing – original draft, Visualization, Validation, Methodology, Investigation, Funding acquisition, Formal analysis, Conceptualization.

Declaration of competing interest

The authors declare that they have no known competing financial interests or personal relationships that could have appeared to influence the work reported in this paper.

Acknowledgement

The present work was supported by the Romanian National Grant GNAC ARUT 2023 project (No. 7/06.10.2023), NANO_NP_DES, entitled "Electrochemical synthesis of hybrid nanoparticles Ag/TiO₂ and Ag/Fe₃O₄ with biomedical applications". Also, the work was supported by the IMT Core Program μ NanoEl, within the PNCDI 2022-2026, carried out with the support of Romanian Ministry of Research, Innovation and Digitization, project No. 23070201.

N.D. acknowledges the support by the contract PN 23 21 01 06 sponsored by the Romanian Ministry of Research, Innovation, and Digitization.

Additionally, National and European funds financially supported the work through FCT under Research Grant UIDB/00081/2020 (<https://doi.org/10.54499/UIDB/00081/2020>)- CIQUP, LA/P/0056/2020 (<https://doi.org/10.54499/LA/P/0056/2020>) – IMS.

Supplementary materials

Supplementary material associated with this article can be found, in the online version, at [doi:10.1016/j.apsadv.2025.100749](https://doi.org/10.1016/j.apsadv.2025.100749).

Data availability

No data was used for the research described in the article.

References

- [1] W. Zhao, Z. Zhang, J. Zhang, H. Wu, L. Xi, C. Ruan, Synthesis of Ag/TiO₂/graphene and its photocatalytic properties under visible light, *Mater. Lett.* 171 (2016) 182–186, <https://doi.org/10.1016/j.matlet.2016.02.063>.
- [2] P.Ch. Dey, R. Das, Enhanced photocatalytic degradation of methyl orange dye on interaction with synthesized ligand free CdS nanocrystals under visible light illumination, *Spectrochim. Acta a Mol. Biomol. Spectrosc.* 231 (2020) 118122, <https://doi.org/10.1016/j.saa.2020.118122>.
- [3] M.F. Hanafi, N. Sapawe, Influence of pH on the photocatalytic degradation of methyl orange using nickel catalyst, *Mater. Today Proc.* 31 (2020) 339–341, <https://doi.org/10.1016/j.matpr.2020.06.094>.
- [4] V.A. Gómez-Obando, A.-M. García-Mora, J.S. Basante, A. Hidalgo, L.-A. Galeano, CWPO degradation of methyl orange at circumneutral pH: multi-response statistical optimization, main intermediates and by-products, *Front. Chem.* 7 (2019), <https://doi.org/10.3389/fchem.2019.00772>.
- [5] G. Durango-Giraldo, A. Cardona, J.F. Zapata, J.F. Santa, R. Buitrago-Sierra, Titanium dioxide modified with silver by two methods for bactericidal applications, *Heliyon.* 5 (2019), <https://doi.org/10.1016/j.heliyon.2019.e01608>.
- [6] M. Sultana, A. Mondal, S. Islam, MOST.A. Khatun, Md.H. Rahaman, A. K. Chakraborty, Md.S. Rahman, M.M. Rahman, A.S.M. Nur, Strategic development of metal doped TiO₂ photocatalysts for enhanced dye degradation activity under UV-Vis irradiation: a review, *Current Research in Green and Sustainable Chemistry* 7 (2023) 100383, <https://doi.org/10.1016/j.crgsc.2023.100383>.
- [7] B.-G. Park, Photocatalytic activity of TiO₂-doped Fe, Ag, and Ni with N under visible light irradiation, *Gels.* 8 (2021) 14, <https://doi.org/10.3390/gels8010014>.
- [8] R. Rescigno, O. Sacco, V. Venditto, A. Fusco, G. Donnarumma, M. Lettieri, R. Fittipaldi, V. Vaiano, Photocatalytic activity of P-doped TiO₂ photocatalyst, *Photochemical & Photobiological Sciences* 22 (2023) 1223–1231, <https://doi.org/10.1007/s43630-023-00363-y>.
- [9] B. Naik, C.H. Manoranjan, A. Chandrashekar, A. Iyer, V.S. Prasad, N.N. Ghosh, Preparation of TiO₂, Ag-doped TiO₂ nanoparticle and TiO₂-SBA-15 nanocomposites using simple aqueous solution-based chemical method and study of their photocatalytic activity, *J. Exp. Nanosci.* 8 (2013) 462–479, <https://doi.org/10.1080/17458080.2011.597435>.
- [10] T.-D. Pham, B.-K. Lee, Effects of Ag doping on the photocatalytic disinfection of *E. coli* in bioaerosol by Ag-TiO₂/GF under visible light, *J. Colloid. Interface Sci.* 428 (2014) 24–31, <https://doi.org/10.1016/j.jcis.2014.04.030>.
- [11] S.P. Deshmukh, S.B. Mullani, V.B. Koli, S.M. Patil, P.J. Kasabe, P.B. Dandge, S. A. Pawar, S.D. Delekar, Ag nanoparticles connected to the surface of TiO₂ electrostatically for antibacterial photoinactivation studies, *Photochem. Photobiol.* 94 (2018) 1249–1262, <https://doi.org/10.1111/php.12983>.
- [12] T. Rahmawati, T. Butburee, W. Sangkhun, T. Wutikhun, J. Padchasi, P. Kidkhunthod, S. Phomma, T. Eksangsri, W. Kangwansapamonkon, P. Leeladee, C. Sapcharoenkun, Green synthesis of Ag-TiO₂ nanoparticles using turmeric extract and its enhanced photocatalytic activity under visible light, *Colloids. Surf. a Physicochem. Eng. Asp.* 665 (2023) 131206, <https://doi.org/10.1016/j.colsurfa.2023.131206>.
- [13] J. Wang, L. Svoboda, Z. Němečková, M. Sgarzi, J. Henych, N. Licciardello, G. Cumiberti, Enhanced visible-light photodegradation of fluoroquinolone-based antibiotics and *E. coli* growth inhibition using Ag-TiO₂ nanoparticles, *RSC. Adv.* 11 (2021) 13980–13991, <https://doi.org/10.1039/D0RA10403E>.
- [14] M.A. Muflikh, M.C. Frommelt, M. Farman, A.Y. Chua, G.N.C. Santos, Structures, mechanical properties and antibacterial activity of Ag/TiO₂ nanocomposite materials synthesized via HVPG technique for coating application, *Heliyon.* 5 (2019), <https://doi.org/10.1016/j.heliyon.2019.e01475>.
- [15] B. Moongraksathum, M.-Y. Chien, Y.-W. Chen, Antiviral and antibacterial effects of silver-doped TiO₂ prepared by the peroxo sol-gel method, *J. Nanosci. Nanotechnol.* 19 (2019) 7356–7362, <https://doi.org/10.1166/jnn.2019.16615>.
- [16] V.H. Rathi, A.R. Jeice, K. Jayakumar, Green synthesis of Ag/CuO and Ag/TiO₂ nanoparticles for enhanced photocatalytic dye degradation, antibacterial, and antifungal properties, *Applied Surface Science Advances* 18 (2023) 100476, <https://doi.org/10.1016/j.apsadv.2023.100476>.
- [17] M.I. Din, R. Khalid, Photocatalysis of pharmaceuticals and organic dyes in the presence of silver-doped TiO₂ photocatalyst—A critical review, *Int. J. Environ. Anal. Chem.* (2023) 1–25, <https://doi.org/10.1080/03067319.2023.2258795>.
- [18] H. Chakhtouna, H. Benzaid, N. Zari, A. el kacem Qaiss, R. Bouhfid, Recent progress on Ag/TiO₂ photocatalysts: photocatalytic and bactericidal behaviors, *Environmental Science and Pollution Research* 28 (2021) 44638–44666, <https://doi.org/10.1007/s11356-021-14996-y>.
- [19] D. Kanakaraju, F.D. anak Kutiang, Y.C. Lim, P.S. Goh, Recent progress of Ag/TiO₂ photocatalyst for wastewater treatment: doping, co-doping, and green materials functionalization, *Appl. Mater. Today* 27 (2022) 101500, <https://doi.org/10.1016/j.apmt.2022.101500>.
- [20] Q. Xiang, J. Yu, B. Cheng, H.C. Ong, Microwave-hydrothermal preparation and visible-light photoactivity of plasmonic photocatalyst Ag-TiO₂ nanocomposite hollow spheres, *Chem. Asian J.* 5 (2010) 1466–1474, <https://doi.org/10.1002/asia.200900695>.

- [21] H.-Y. Jung, I.-S. Yeo, T.-U. Kim, H.-C. Ki, H.-B. Gu, Surface plasmon resonance effect of silver nanoparticles on a TiO₂ electrode for dye-sensitized solar cells, *Appl. Surf. Sci.* 432 (2018) 266–271, <https://doi.org/10.1016/j.apsusc.2017.04.237>.
- [22] D. Mangalaraj, D. Nithya Devi, Ag/TiO₂ (metal/metal oxide) core shell nanoparticles for biological applications. *Recent Trends in Materials Science and Applications*, Springer, 2017, pp. 9–17, https://doi.org/10.1007/978-3-319-44890-9_2.
- [23] C. Zarzeka, J. Goldoni, J. do R. de Paula de Oliveira, G.G. Lenzi, M.D. Bagatini, L. M.S. Colpini, Photocatalytic action of Ag/TiO₂ nanoparticles to emerging pollutants degradation: a comprehensive review, *Sustainable Chemistry for the Environment* 8 (2024) 100177, <https://doi.org/10.1016/j.senv.2024.100177>.
- [24] H. Mao, Z. Fei, C. Bian, L. Yu, S. Chen, Y. Qian, Facile synthesis of high-performance photocatalysts based on Ag/TiO₂ composites, *Ceram. Int.* 45 (2019) 12586–12589, <https://doi.org/10.1016/j.ceramint.2019.03.109>.
- [25] S. Abbas, K. Guergouri, S. Gazaout, S. Djebabra, A. Zertal, R. Barille, M. Zaabat, Effect of silver doping on the photocatalytic activity of TiO₂ nanopowders synthesized by the sol-gel route, *J. Environ. Chem. Eng.* 8 (2020) 103718, <https://doi.org/10.1016/j.jece.2020.103718>.
- [26] A. Evcin, E. Arlı, Z. Baz, R. Eesen, E.G. Sever, Characterization of Ag-TiO₂ powders prepared by sol-gel process, *Acta Phys. Pol. a* 132 (2017) 608–611, <https://doi.org/10.12693/APhysPolA.132.608>.
- [27] M. Harikishore, M. Sandhyarani, K. Venkateswarlu, T.A. Nellaippan, N. Rameshbabu, Effect of Ag doping on antibacterial and photocatalytic activity of nanocrystalline TiO₂, *Procedia Materials Science* 6 (2014) 557–566, <https://doi.org/10.1016/j.mspro.2014.07.071>.
- [28] R. Saravanan, D. Manoj, J. Qin, Mu. Naushad, F. Gracia, A.F. Lee, M.M. Khan, M. A. Gracia-Pinilla, Mechanochemical synthesis of Ag/TiO₂ for photocatalytic methyl orange degradation and hydrogen production, *Process Safety and Environmental Protection* 120 (2018) 339–347, <https://doi.org/10.1016/j.psep.2018.09.015>.
- [29] G. Suriati, M. Mariatti, A. Azizan, Synthesis of silver nanoparticles by chemical reduction method: effect of reducing agent and surfactant concentration, *International Journal of Automotive and Mechanical Engineering* 10 (2022) 1920–1927, <https://doi.org/10.15282/ijame.10.2014.9.0160>.
- [30] M. Hussain, S. Tariq, M. Ahmad, H. Sun, K. Maaz, G. Ali, S.Z. Hussain, M. Iqbal, S. Karim, A. Nisar, Ag/TiO₂ nanocomposite for environmental and sensing applications, *Mater. Chem. Phys.* 181 (2016) 194–203, <https://doi.org/10.1016/j.matchemphys.2016.06.049>.
- [31] H. Iino, N. Yamauchi, K. Nakashima, K. Watanabe, H. Koda, H. Kunigami, H. Kunigami, Y. Kobayashi, Electrolytic synthesis of metallic zinc nanoparticles, *Journal of Nanoparticle Research* 23 (2021) 46, <https://doi.org/10.1007/s11051-021-05160-1>.
- [32] Z. Huang, H. Jiang, P. Liu, J. Sun, D. Guo, J. Shan, N. Gu, Continuous synthesis of size-tunable silver nanoparticles by a green electrolysis method and multi-electrode design for high yield, *J. Mater. Chem. a Mater.* 3 (2015) 1925–1929, <https://doi.org/10.1039/C4TA06782G>.
- [33] R. Singaravelan, S. Bangaru Sudarsan Alwar, Electrochemical synthesis, characterisation and phytochemical properties of silver nanoparticles, *Appl. Nanosci.* 5 (2015) 983–991, <https://doi.org/10.1007/s13204-014-0396-0>.
- [34] V.-T. Hoang, N.X. Dinh, T.N. Pham, T.V. Hoang, P.A. Tuan, T.Q. Huy, A.-T. Le, Scalable electrochemical synthesis of novel biogenic silver nanoparticles and its application to high-sensitive detection of 4-nitrophenol in aqueous system, *Advances in Polymer Technology* 2021 (2021) 1–9, <https://doi.org/10.1155/2021/6646219>.
- [35] M.S. Chandrasekar, M. Pushpavanam, Pulse and pulse reverse plating—Conceptual, advantages and applications, *Electrochim. Acta* 53 (2008) 3313–3322, <https://doi.org/10.1016/j.electacta.2007.11.054>.
- [36] Steve Koelzer, *Pulse plating back to basics: pulse math, Plating and Surface Finishing* (2000) 52–53.
- [37] E. Mariani, W. Giurlani, M. Bonechi, V. Dell'Aquila, M. Innocenti, A systematic study of pulse and pulse reverse plating on acid copper bath for decorative and functional applications, *Sci. Rep.* 12 (2022) 18175, <https://doi.org/10.1038/s41598-022-22650-x>.
- [38] D. Yin, Y. Liu, P. Chen, G. Meng, G. Huang, L. Cai, L. Zhang, Controllable synthesis of silver nanoparticles by the pulsed electrochemical deposition in a forced circulation reactor, *Int. J. Electrochem. Sci.* 15 (2020) 3469–3478, <https://doi.org/10.20964/2020.04.57>.
- [39] S.A. Lee, J.W. Yang, S. Choi, H.W. Jang, Nanoscale electrodeposition: dimension control and 3D conformality, *Exploration* 1 (2021), <https://doi.org/10.1002/EXP.20210012>.
- [40] D. Wang, Z.-H. Zhou, H. Yang, K.-B. Shen, Y. Huang, S. Shen, Preparation of TiO₂ loaded with crystalline nano Ag by a one-step low-temperature hydrothermal method, *J. Mater. Chem.* 22 (2012) 16306, <https://doi.org/10.1039/c2jm16217b>.
- [41] A. Azzouz, M. Hayyan, Potential applications of deep eutectic solvents in nanotechnology: part II, *Chemical Engineering Journal* 468 (2023) 143563, <https://doi.org/10.1016/j.cej.2023.143563>.
- [42] B.B. Hansen, S. Spittle, B. Chen, D. Poe, Y. Zhang, J.M. Klein, A. Horton, L. Adhikari, T. Zelovich, B.W. Doherty, B. Gurkan, E.J. Maginn, A. Ragauskas, M. Dammun, T.A. Zawodzinski, G.A. Baker, M.E. Tuckerman, R.F. Savinell, J. R. Sangoro, Deep eutectic solvents: a review of fundamentals and applications, *Chem. Rev.* 121 (2021) 1232–1285, <https://doi.org/10.1021/acs.chemrev.0c00385>.
- [43] S. Sugiarto, U. Aloka Weerasinghe, J. Kinyanjui Muiruri, A. Yu Qing Chai, J. Chee Chuan Yeo, G. Wang, Q. Zhu, X. Jun Loh, Z. Li, D. Kai, Nanomaterial synthesis in deep eutectic solvents, *Chemical Engineering Journal* 499 (2024) 156177, <https://doi.org/10.1016/j.cej.2024.156177>.
- [44] A.T.S.C. Brandão, S. Rosoiu, R. Costa, O.A. Lazar, A.F. Silva, L. Anicai, C. M. Pereira, M. Enachescu, Characterization and electrochemical studies of MWCNTs decorated with Ag nanoparticles through pulse reversed current electrodeposition using a deep eutectic solvent for energy storage applications, *J. Mater. Res. Technol.* 15 (2021) 342–359, <https://doi.org/10.1016/j.jmrt.2021.08.031>.
- [45] L. Anicai, A. Petica, D. Patroi, V. Marinescu, P. Prioteasa, S. Costovici, Electrochemical synthesis of nanosized TiO₂ nanopowder involving choline chloride based ionic liquids, *Materials Science and Engineering: B* 199 (2015) 87–95, <https://doi.org/10.1016/j.mseb.2015.05.005>.
- [46] A. Joseph, B. Kirubasankar, A.M. Mathew, M. Narayanasamy, C. Yan, S. Angaiah, Influence of pulse reverse current parameters on electrodeposition of copper-graphene nanocomposite coating, *Applied Surface Science Advances* 5 (2021) 100116, <https://doi.org/10.1016/j.apsadv.2021.100116>.
- [47] S.P. State, S. Costovici, M. Mousavi, Y.G. Garcia, C. Zanella, A. Cojocar, L. Anicai, T. Visan, M. Enachescu, Electrodeposited Sn-Cu-Ni alloys as lead-free solders on copper substrate using deep eutectic solvents: the influence of electrodeposition mode on the morphology, composition and corrosion behaviour, *Surf. Coat. Technol.* (2023) 130324, <https://doi.org/10.1016/j.surfcoat.2023.130324>.
- [48] S.P. Rosoiu, A.G. Pantazi, A. Petica, A. Cojocar, S. Costovici, C. Zanella, T. Visan, L. Anicai, M. Enachescu, Electrodeposition of NiSn-rGO composite coatings from deep eutectic solvents and their physicochemical characterization, *Metals* (Basel) 10 (2020) 1–21, <https://doi.org/10.3390/met10111455>.
- [49] S.P. Rosoiu, A.G. Pantazi, A. Petica, A. Cojocar, S. Costovici, C. Zanella, T. Visan, L. Anicai, M. Enachescu, Comparative study of Ni-Sn alloys electrodeposited from choline chloride-based ionic liquids in direct and pulsed current, *Coatings* 9 (2019) 1–15, <https://doi.org/10.3390/coatings9120801>.
- [50] N. Fairley, V. Fernandez, M. Richard-Plouet, C. Guillot-Deudon, J. Walton, E. Smith, D. Flahaut, M. Greiner, M. Biesinger, S. Tougaard, D. Morgan, J. Baltrusaitis, Systematic and collaborative approach to problem solving using X-ray photoelectron spectroscopy, *Applied Surface Science Advances* 5 (2021) 100112, <https://doi.org/10.1016/j.apsadv.2021.100112>.
- [51] C. Chen, Y. Zhao, T. Lei, D. Yang, Y. Zhou, J. Zeng, R. Xie, W. Hu, F. Dong, Photocatalytic mechanism conversion of titanium dioxide induced via surface interface coordination, *Chemosphere* 309 (2022) 136745, <https://doi.org/10.1016/j.chemosphere.2022.136745>.
- [52] M.T. Reetz, W. Helbig, Size-selective synthesis of nanostructured transition metal clusters, *J. Am. Chem. Soc.* 116 (1994) 7401–7402, <https://doi.org/10.1021/ja00095a051>.
- [53] B. Yin, H. Ma, S. Wang, S. Chen, Electrochemical synthesis of silver nanoparticles under protection of poly(*N*-vinylpyrrolidone), *J. Phys. Chem. B* 107 (2003) 8898–8904, <https://doi.org/10.1021/jp0349031>.
- [54] A.T.S.C. Brandão, S. Rosoiu, R. Costa, A. Fernando Silva, L. Anicai, M. Enachescu, C.M. Pereira, Characterization of carbon nanomaterials dispersions: can metal decoration of MWCNTs improve their physicochemical properties? *Nanomaterials* 12 (2022) <https://doi.org/10.3390/nano12010099>.
- [55] A.T.S.C. Brandão, S. Rosoiu, R. Costa, A.F. Silva, L. Anicai, C.M. Pereira, M. Enachescu, Dispersion stability of MWCNTs decorated with Ag nanoparticles through pulse-reversed current electrodeposition using a deep eutectic solvent, (2022) 29, <https://doi.org/10.3390/materproc2022009029>.
- [56] H.M. Rietveld, A profile refinement method for nuclear and magnetic structures, *J. Appl. Crystallogr.* 2 (1969) 65–71, <https://doi.org/10.1107/s0021889869006558>.
- [57] A.D. French, Idealized powder diffraction patterns for cellulose polymorphs, *Cellulose* 21 (2014) 885–896, <https://doi.org/10.1007/s10570-013-0030-4>.
- [58] P.Y.Z. Vitalij, K. Pecharsky, *Fundamentals of Powder Diffraction and Structural Characterization of Materials*, 2nd ed., Springer US, Boston, MA, 2009 <https://doi.org/10.1007/978-0-387-09579-0>.
- [59] P. Pascariu, C. Cojocar, M. Homocianu, P. Samoila, C. Romanitan, D. Nikolay, Electrospun Sn-doped TiO₂: synthesis, structural, optical and catalytic performance as a function of Sn loading and calcination temperatures, *Ceram. Int.* 49 (2023) 10384–10394, <https://doi.org/10.1016/j.ceramint.2022.11.219>.
- [60] C. Romanitan, I.V. Tudose, K. Mouratis, M.C. Popescu, C. Pachi, S. Couris, E. Koudoumas, M. Suche, Structural investigations in electrochromic vanadium pentoxide thin films, *Physica Status Solidi* 219 (2022), <https://doi.org/10.1002/pssa.202100431>.
- [61] M. Aroyo, N. Tzonev, *Pulse periodic reverse plating- new possibilities for electrodeposition of metal coatings with improved properties: part 1, Plating & Surface Finishing* (2002) 48–53.
- [62] A.N. Al-Hakimi, T.M. Alreshedi, R.A. Albarrak, The effect of the Saudi haloxylon ammodendron shrub on silver nanoparticles: optimal biosynthesis, characterization, removability of mercury ions, antimicrobial and anticancer activities, *Inorganics* (Basel) 11 (2023) 246, <https://doi.org/10.3390/inorganics11060246>.
- [63] S. Elyamny, M. Eltarahony, M. Abu-Serie, M.M. Nabil, A.E.-H.B. Kashyout, One-pot fabrication of Ag@Ag₂O core-shell nanostructures for biosafe antimicrobial and antibiofilm applications, *Sci. Rep.* 11 (2021) 22543, <https://doi.org/10.1038/s41598-021-01687-4>.
- [64] Z.H. Dhoondia, H. Chakraborty, *Lactobacillus* mediated synthesis of silver oxide nanoparticles, *Nanomaterials and Nanotechnology* 2 (2012) 15, <https://doi.org/10.5772/55741>.
- [65] S.I. Mogal, V.G. Gandhi, M. Mishra, S. Tripathi, T. Shripathi, P.A. Joshi, D.O. Shah, Single-step synthesis of silver-doped titanium dioxide: influence of silver on structural, textural, and photocatalytic properties, *Ind. Eng. Chem. Res.* 53 (2014) 5749–5758, <https://doi.org/10.1021/ie404230q>.

- [66] B. Chinnam, C.S. Dasagiri, R. Araga, Synthesis and preliminary evaluation of Ag-TiO₂/CNT hybrid nanocomposite for the degradation of polystyrene microplastics under solar irradiation, *Environmental Science and Pollution Research* 31 (2024) 32863–32874, <https://doi.org/10.1007/s11356-024-33438-z>.
- [67] P. Tzevelekidis, M. Theodosiou, A. Papadopoulou, E. Sakellis, N. Boukos, A. K. Bikogiannakis, G. Kyriakou, E.K. Efthimiadou, C.A. Mitsopoulou, Visible-light-activated antibacterial and antipollutant properties of biocompatible Cu-doped and Ag-decorated TiO₂ nanoparticles, *Heliyon*. 10 (2024) e35634, <https://doi.org/10.1016/j.heliyon.2024.e35634>.
- [68] S.W. Gaarenstroom, N. Winograd, Initial and final state effects in the ESCA spectra of cadmium and silver oxides, *J. Chem. Phys.* 67 (1977) 3500–3506, <https://doi.org/10.1063/1.435347>.
- [69] G.B. Hoflund, Z.F. Hazos, G.N. Salaita, Surface characterization study of Ag, Ag₂O, and Ag₂O using x-ray photoelectron spectroscopy and electron energy-loss spectroscopy, *Phys. Rev. B* 62 (2000) 11126–11133, <https://doi.org/10.1103/PhysRevB.62.11126>.
- [70] W. Wei, D. Yu, Q. Huang, Preparation of Ag/TiO₂ nanocomposites with controlled crystallization and properties as a multifunctional material for SERS and photocatalytic applications, *Spectrochim. Acta a Mol. Biomol. Spectrosc.* 243 (2020) 118793, <https://doi.org/10.1016/j.saa.2020.118793>.
- [71] C.A. Castro, A. Jurado, D. Sissa, S.A. Giraldo, Performance of Ag-TiO₂ photocatalysts towards the photocatalytic disinfection of water under interior-lighting and solar-simulated light irradiations, *International Journal of Photoenergy* 2012 (2012) 1–10, <https://doi.org/10.1155/2012/261045>.
- [72] Q. Wu, M. Si, B. Zhang, K. Zhang, H. Li, L. Mi, Y. Jiang, Y. Rong, J. Chen, Y. Fang, Strong damping of the localized surface plasmon resonance of Ag nanoparticles by Ag₂O, *Nanotechnology*. 29 (2018) 295702, <https://doi.org/10.1088/1361-6528/aac031>.
- [73] P. Pascariu, C. Cojocaru, N. Olaru, P. Samoila, A. Airinei, M. Ignat, L. Sacarescu, D. Timpu, Novel rare earth (RE-La, Er, Sm) metal doped ZnO photocatalysts for degradation of Congo-Red dye: synthesis, characterization and kinetic studies, *J. Environ. Manage* 239 (2019) 225–234, <https://doi.org/10.1016/j.jenvman.2019.03.060>.
- [74] S. Sharma, B. Devi, D. Koiri, K. Sharma, K.G. Bhattacharyya, A. Devi, Visible light photocatalytic degradation of methylene blue and rhodamine B over silver-doped titanium dioxide nanocomposites supported on Fuller's earth, *Environ. Monit. Assess.* 195 (2023) 1362, <https://doi.org/10.1007/s10661-023-11981-5>.
- [75] S. Elbasaney, A.M. El-Khawaga, M.A. Elsayed, M.A. Correa-Duarte, Silver doped anatase nanocomposite: a novel photocatalyst with advanced activity under visible light for waste-water treatment, *Discover Applied Sciences* 6 (2024) 159, <https://doi.org/10.1007/s42452-024-05804-6>.
- [76] M. Kunnamareddy, B. Diravidamani, R. Rajendran, B. Singaram, K. Varadharajan, Synthesis of silver and sulphur codoped TiO₂ nanoparticles for photocatalytic degradation of methylene blue, *Journal of Materials Science: Materials in Electronics* 29 (2018) 18111–18119, <https://doi.org/10.1007/s10854-018-9922-2>.
- [77] N. Aini, S. Rachman, A. Maunatin, A. Syarifah, Synthesis, characterization and antibacterial activity of silver doped TiO₂ photocatalyst, in: *AIP Conf. Proc.* 2019 050017, <https://doi.org/10.1063/1.5115693>.
- [78] S. Kader, Md.R. Al-Mamun, Md.B.K. Suhan, S.B. Shuchi, Md.S. Islam, Enhanced photodegradation of methyl orange dye under UV irradiation using MoO₃ and Ag doped TiO₂ photocatalysts, *Environ. Technol. Innov.* 27 (2022) 102476, <https://doi.org/10.1016/j.eti.2022.102476>.
- [79] H. Wang, G. Wang, Y. Zhang, Y. Ma, Z. Wu, D. Gao, R. Yang, B. Wang, X. Qi, J. Yang, Preparation of RGO/TiO₂/Ag aerogel and its photodegradation performance in gas phase formaldehyde, *Sci. Rep.* 9 (2019) 16314, <https://doi.org/10.1038/s41598-019-52541-7>.
- [80] H.-T. Ren, Q. Yang, Fabrication of Ag₂O/TiO₂ with enhanced photocatalytic performances for dye pollutants degradation by a pH-induced method, *Appl. Surf. Sci.* 396 (2017) 530–538, <https://doi.org/10.1016/j.apsusc.2016.10.191>.
- [81] T. Rahmawati, T. Butburee, W. Sangkhun, T. Wutikhun, J. Padchasi, P. Kidkhunthod, S. Phromma, T. Eksangsri, W. Kangwansupamonkon, P. Leeladee, C. Sapcharoenkun, Green synthesis of Ag-TiO₂ nanoparticles using turmeric extract and its enhanced photocatalytic activity under visible light, *Colloids. Surf. a Physicochem. Eng. Asp.* 665 (2023) 131206, <https://doi.org/10.1016/j.colsurfa.2023.131206>.
- [82] A. Petica, A. Florea, C. Gaidau, D. Balan, L. Anicai, Synthesis and characterization of silver-titania nanocomposites prepared by electrochemical method with enhanced photocatalytic characteristics, antifungal and antimicrobial activity, *J. Mater. Res. Technol.* 8 (2019) 41–53, <https://doi.org/10.1016/j.jmrt.2017.09.009>.
- [83] T.H. Nguyen, N.H. Hoang, C. Van Tran, P.T.M. Nguyen, T.-D. Dang, W.J. Chung, S. W. Chang, D.D. Nguyen, P. Senthil Kumar, D.D. La, Green synthesis of a photocatalyst Ag/TiO₂ nanocomposite using Cleistocalyx operculatus leaf extract for degradation of organic dyes, *Chemosphere* 306 (2022) 135474, <https://doi.org/10.1016/j.chemosphere.2022.135474>.
- [84] H.M. Sung-Suh, J.R. Choi, H.J. Hah, S.M. Koo, Y.C. Bae, Comparison of Ag deposition effects on the photocatalytic activity of nanoparticulate TiO₂ under visible and UV light irradiation, *J. Photochem. Photobiol. a Chem.* 163 (2004) 37–44, [https://doi.org/10.1016/S1010-6030\(03\)00428-3](https://doi.org/10.1016/S1010-6030(03)00428-3).
- [85] K.S. Landage, G.K. Arbade, P. Khanna, C.J. Bhongale, Biological approach to synthesize TiO₂ nanoparticles using Staphylococcus aureus for antibacterial and antibiofilm applications, *J. Microbiol. Exp.* 8 (2020) 36–43, <https://doi.org/10.15406/jmen.2020.08.00283>.
- [86] Y. Yuan, J. Ding, J. Xu, J. Deng, J. Guo, TiO₂ nanoparticles co-doped with silver and nitrogen for antibacterial application, *J. Nanosci. Nanotechnol.* 10 (2010) 4868–4874, <https://doi.org/10.1166/jnn.2010.2225>.
- [87] C. López de Castillo, M.Guerrero Correa, F.B. Martínez, C. Streitt, M.José Galotto, Antimicrobial effect of titanium dioxide nanoparticles. *Antimicrobial Resistance - A One Health Perspective*, IntechOpen, 2021, <https://doi.org/10.5772/intechopen.90891>.
- [88] H. Zhang, G. Chen, Potent antibacterial activities of Ag/TiO₂ nanocomposite powders synthesized by a one-pot sol-gel method, *Environ. Sci. Technol.* 43 (2009) 2905–2910, <https://doi.org/10.1021/es803450f>.
- [89] S.A.H. Jalali, A.R. Allafchian, S.S. Banifatemi, I.Ashrafi Tamai, The antibacterial properties of Ag/TiO₂ nanoparticles embedded in silane sol-gel matrix, *J. Taiwan. Inst. Chem. Eng.* 66 (2016) 357–362, <https://doi.org/10.1016/j.jtice.2016.06.011>.
- [90] I. Carvalho, S. Fervod, C. Mansilla, S.M. Marques, M.A. Cerqueira, L.M. Pastrana, M. Henriques, C. Gaidau, P. Ferreira, S. Carvalho, Development of antimicrobial leather modified with Ag-TiO₂ nanoparticles for footwear industry, *Science and Technology of Materials* 30 (2018) 60–68, <https://doi.org/10.1016/j.stmat.2018.09.002>.
- [91] W. Zhang, T. Jiang, N. Li, S. Zhao, Y. Zhao, Enhanced photocatalytic degradation of methyl orange by metal-tio₂ nanoparticles, *ChemistrySelect.* 9 (2024), <https://doi.org/10.1002/slct.202401814>.
- [92] Y. Song, H. Li, Z. Xiong, L. Cheng, M. Du, Z. Liu, J. Li, D. Li, TiO₂/carbon composites from waste sawdust for methylene blue photodegradation, *Diam. Relat. Mater.* 136 (2023) 109918, <https://doi.org/10.1016/j.diamond.2023.109918>.
- [93] Q. Jiang, S. Wang, X. Li, Z. Han, C. Zhao, T. Di, S. Liu, Z. Cheng, Controllable growth of MoS₂ nanosheets on TiO₂ burst nanotubes and their photocatalytic activity, *RSC. Adv.* 10 (2020) 40904–40915, <https://doi.org/10.1039/D0RA08421B>.
- [94] T. Vembuli, S. Thiripuranthagan, T. Sureshkumar, E. Erusappan, S. Kumaravel, M. Kasinathan, B. Natesan, A. Sivakumar, Degradation of harmful organics using visible light driven N-TiO₂/rGO nanocomposite, *J. Nanosci. Nanotechnol.* 21 (2021) 3081–3091, <https://doi.org/10.1166/jnn.2021.19122>.
- [95] K.H. Leong, B.L. Gan, S. Ibrahim, P. Saravanan, Synthesis of surface plasmon resonance (SPR) triggered Ag/TiO₂ photocatalyst for degradation of endocrine disturbing compounds, *Appl. Surf. Sci.* 319 (2014) 128–135, <https://doi.org/10.1016/j.apsusc.2014.06.153>.
- [96] R. Gang, Y. Xia, L. Xu, L. Zhang, S. Ju, Z. Wang, S. Koppala, Size controlled Ag decorated TiO₂ plasmonic photocatalysts for tetracycline degradation under visible light, *Surf. Interfaces.* 31 (2022) 102018, <https://doi.org/10.1016/j.surfin.2022.102018>.